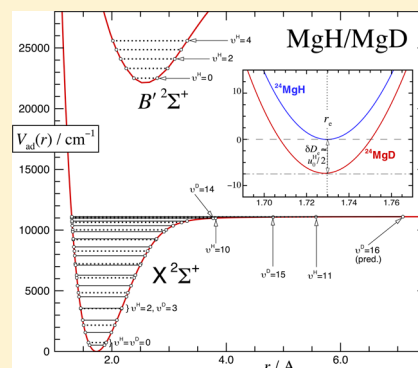


Accurate Analytic Potential and Born–Oppenheimer Breakdown Functions for MgH and MgD from a Direct-Potential-Fit Data Analysis

Robert D. E. Henderson,^{*,†,‡} Alireza Shayesteh,^{†,§} Jason Tao,[†] Carl C. Haugen,[†] Peter F. Bernath,^{†,||} and Robert J. Le Roy^{*,†}[†]Department of Chemistry, University of Waterloo, Waterloo, Ontario N2L 3G1, Canada[‡]Department of Physics and Astronomy, University of Waterloo, Waterloo, Ontario N2L 3G1, Canada

S Supporting Information

ABSTRACT: New high-resolution visible Fourier transform emission spectra of the $A\ ^2\Pi \rightarrow X\ ^2\Sigma^+$ and $B'\ ^2\Sigma^+ \rightarrow X\ ^2\Sigma^+$ systems of ^{24}MgD and of the $B'\ ^2\Sigma^+ \rightarrow X\ ^2\Sigma^+$ systems of $^{25,26}\text{MgD}$ and $^{25,26}\text{MgH}$ have been combined with earlier results for ^{24}MgH in a multi-isotopologue direct-potential-fit analysis to yield improved analytic potential energy and Born–Oppenheimer breakdown functions for the ground $X\ ^2\Sigma^+$ state of MgH. Vibrational levels of the ground state of ^{24}MgD were observed up to $v'' = 15$, which is bound by only $30.6 \pm 0.10\text{ cm}^{-1}$. Including deuteride and minor magnesium isotopologue data allowed us also to determine the adiabatic Born–Oppenheimer breakdown effects in this molecule. The fitting procedure used the recently developed Morse/Long-Range (MLR) potential energy function, whose asymptotic behavior incorporates the correct inverse-power form. A spin-splitting radial correction function to take account of the $^2\Sigma$ spin–rotation interaction was also determined. Our refined value for the ground-state dissociation energy of the dominant isotopologue (^{24}MgH) is $\mathcal{D}_e = 11\,104.25 \pm 0.8\text{ cm}^{-1}$, in which the uncertainty also accounts for the model dependence of the fitted \mathcal{D}_e values for a range of physically acceptable fits. We were also able to determine the marked difference in the well depths of ^{24}MgH and ^{24}MgD (with the deuteride potential curve being $7.58 \pm 0.30\text{ cm}^{-1}$ deeper than that of the hydride) as well as smaller well-depth differences for the minor $^{25,26}\text{Mg}$ isotopologues. This analytic potential function also predicts that the highest bound level of ^{24}MgD is $v'' = 16$ and that it is bound by only $2.73 \pm 0.10\text{ cm}^{-1}$.



I. INTRODUCTION

In studies involving our Milky Way galaxy, magnesium monohydride (MgH) has proven to be a useful tool in the study of stellar atmospheres. In fact, the very first experimental spectrum of MgH was recorded by Fowler in 1907 as part of his efforts to identify several strong bands appearing in sunspot umbrae.¹ Nearly a century later, bands of the $B'\ ^2\Sigma^+ \rightarrow X\ ^2\Sigma^+$ transitions of MgH were used by Wallace et al.² to determine a solar isotope abundance ratio of $^{24}\text{Mg}:^{25}\text{Mg}:^{26}\text{Mg} = 76:12:12$. A similar study was reported a year later by Gay and Lambert,³ who considered 20 different stars of various metallicities ($[\text{Fe}]/[\text{H}]$) with effective temperatures in the range $4190\text{ K} < T_{\text{eff}} < 5350\text{ K}$. They found a general trend in which the abundance of ^{25}Mg and ^{26}Mg relative to that of the major isotope ^{24}Mg decreased with decreasing metallicity. Somewhat earlier, Bonnell and Bell⁴ had used spectral features of MgH to determine the surface gravities of five giant stars of spectral types G and K by matching the magnesium abundance derived from MgH to that found from Mg. For a discussion of other applications of MgH in astronomy, see ref 5, which also reports the use of an early analysis of high-resolution Fourier transform spectroscopy on the $A\ ^2\Pi \rightarrow X\ ^2\Sigma^+$ system to predict purely rotational transition frequencies in the interstellar medium. In addition to its importance in astrophysics, MgH is interesting

from a spectroscopic point of view, with the interacting low-lying excited states $A\ ^2\Pi$ and $B'\ ^2\Sigma^+$ being of particular interest. As will be discussed later, the spectral lines involving transitions from these states into the ground $X\ ^2\Sigma^+$ state are rife with perturbations.

Following Fowler's work,¹ several studies from the 1920s to the 1960s reported on the visible spectrum of MgH and its analysis.^{6–14} In the 1970s, Balfour and collaborators performed an extensive array of studies of low-lying excited states for both ^{24}MgH and ^{24}MgD and measured some ultraviolet spectra.^{15–22} In their early work on MgH, they determined a dissociation energy of $\mathcal{D}_0^{\text{MgH}} = 1.33 \pm 0.06\text{ eV}$ from a Birge–Sponer extrapolation based on data for levels up to $v'' = 6$ observed in the $A\ ^2\Pi \rightarrow X\ ^2\Sigma^+$ spectrum.²⁰ In later work, \mathcal{D}_0 was redetermined to be $1.27 \pm 0.03\text{ eV}$ from data for levels up to $v'' = 6$ obtained from the $B'\ ^2\Sigma^+ \rightarrow X\ ^2\Sigma^+$ spectrum.²¹ The latter estimate of this dissociation energy agreed fairly well with the

Special Issue: Terry A. Miller Festschrift

Received: July 6, 2013

Revised: October 2, 2013

Published: October 4, 2013



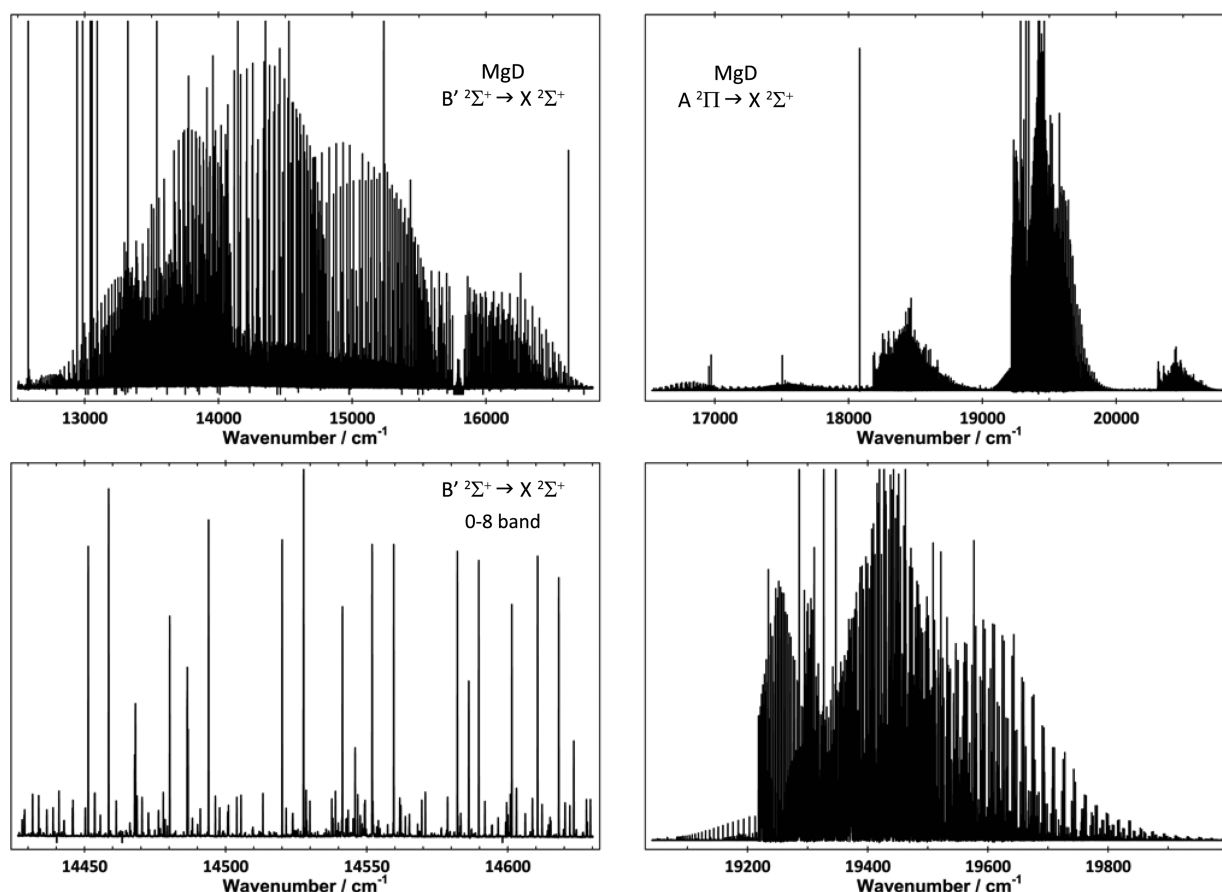


Figure 1. Survey spectra of the (top left) $B' \ ^2\Sigma^+ \rightarrow X \ ^2\Sigma^+$ and (top right) $A \ ^2\Pi \rightarrow X \ ^2\Sigma^+$ systems of MgD. (bottom left) Details of the rotational structure of the $B' \ ^2\Sigma^+ \rightarrow X \ ^2\Sigma^+$ transition, showing the P and R branches of the 0–8 band. (bottom right) Details of the $\Delta\nu = 0$ segment of the $A \ ^2\Pi \rightarrow X \ ^2\Sigma^+$ spectrum.

ab initio value of Meyer and Rosmus,²³ $D_0 = 1.25 \pm 0.05$ eV, and with the present value, $D_0 = 1.285\,11 \pm 0.000\,10$ eV.

In 2004, our group reported²⁴ a multi-isotopologue Dunham-type analysis of the ground $X \ ^2\Sigma^+$ state of MgH using a combination of new Fourier transform infrared emission spectra with previously published microwave and diode-laser vibration–rotation data.^{25–28} Three years later, we reported new data for the $A \rightarrow X$ and $B' \rightarrow X$ transitions of ^{24}MgH and performed a direct-potential-fit (DPF) analysis on the combination of these newer data with all of the previous data.²⁹ This analysis yielded an improved dissociation energy of $1.285\,17 \pm 0.000\,06$ eV. It also enabled the determination of an accurate analytic potential energy curve for the ground state of MgH, from which we computed vibration–rotation band constants for all 12 of its vibrational levels. The work of ref 29 shall henceforth be identified as Paper 1. This analytic potential energy function has also been employed recently for the calculation of Einstein A coefficients for the $A \rightarrow X$ and $B' \rightarrow X$ systems.³⁰

The current paper presents new high-resolution Fourier transform visible emission spectra of the $A \ ^2\Pi \rightarrow X \ ^2\Sigma^+$ and $B' \ ^2\Sigma^+ \rightarrow X \ ^2\Sigma^+$ systems of the deuteride isotopologue of ^{24}MgH as well as the $B' \ ^2\Sigma^+ \rightarrow X \ ^2\Sigma^+$ bands of its (stable) minor magnesium isotopologues. Our spectra of the major deuteride species extends up to $\nu'' = 15$, which is bound by only 0.27% of the well depth. These data are combined with both the previously published microwave²⁸ and infrared²⁴ data for all six isotopologues and the visible spectra of MgH reported in Paper

1 to provide the first combined-isotopologue DPF analysis of this system, as reported herein. The simultaneous treatment of data for multiple isotopologues allows us to delineate adiabatic and nonadiabatic (centrifugal) Born–Oppenheimer breakdown (BOB) effects and to make an accurate determination of the differences between the well depths of the hydride and deuteride and those for the various magnesium isotopologues. We also determine an improved analytic potential energy function for MgH, and an analysis of the model-dependence allows us to obtain more realistic estimates of the uncertainties in those dissociation energies.

In the following, section II presents an overview of the experimental data and a survey of the new deuteride results. Section III then presents details of the improved potential energy function model used in the DPF analysis and of aspects of the fitting procedure. Finally, section IV presents the results of our DPF analysis and section V discusses those results and presents our conclusions.

II. THE DATA

A. Experimental Details Regarding the MgD Spectra.

Although the new MgD spectra were obtained in a manner very similar to that described in Paper 1, we shall provide a brief overview highlighting differences. Optical spectra were obtained using the discharge furnace source described in Paper 1, with approximately 50 g of Mg powder placed in an alumina tube. An initial spectrum was recorded at a temperature of 650 °C with the spectral range limited to 9000–18000 cm^{-1} by using a

550 nm long-wave-pass filter that captured most of the $B' \ ^2\Sigma^+ \rightarrow X \ ^2\Sigma^+$ transitions. The instrumental resolution for this spectrum was 0.0375 cm^{-1} . A second spectrum was then recorded at a temperature of $550 \text{ }^\circ\text{C}$, with an instrumental resolution of 0.065 cm^{-1} and with the spectral range limited to $16000\text{--}23000 \text{ cm}^{-1}$ by employing 450 nm long-wave-pass and 600 nm short-wave-pass filters, thereby capturing most of the $A \ ^2\Pi \rightarrow X \ ^2\Sigma^+$ transitions. The alumina tube cell was filled with a flowing mixture of argon (1.6 Torr) and deuterium (0.2 Torr) for the $9000\text{--}18000 \text{ cm}^{-1}$ spectrum and with pure deuterium (0.5 Torr) for the $16000\text{--}23000 \text{ cm}^{-1}$ spectrum.

Emission was detected by a Bruker IFS 120 HR Fourier transform spectrometer after focusing by a CaF_2 lens. The signal-to-noise ratio (S/N) was greatly enhanced by coadding about 400 scans over several hours; specifically, this yielded $S/N \approx 1000$ for the strongest MgD lines in the spectra. The upper panels of Figure 1 show overviews of the MgD spectra for the $B' \ ^2\Sigma^+ \rightarrow X \ ^2\Sigma^+$ and $A \ ^2\Pi \rightarrow X \ ^2\Sigma^+$ systems.

Transitions involving the hydride minor isotopologues ^{25}MgH and ^{26}MgH were found in the spectra described in Paper 1, and their combination with the analogous results for ^{25}MgD and ^{26}MgD obtained in the present work facilitated making proper line assignments for all of these minor ^{25}Mg and ^{25}Mg data.

Line positions in the spectra were measured using the program WSpecra written by M. Carleer (Université Libre de Bruxelles). To obtain vacuum wavenumbers, the correction formula given in ref 31 was applied. Absolute wavenumber calibrations for the $B' \ ^2\Sigma^+ \rightarrow X \ ^2\Sigma^+$ lines were derived from atomic lines of argon previously reported by Norlen.³² However, following the recommendation of a more recent study of argon emission lines in a hollow cathode discharge lamp,³³ the argon line energies reported in ref 32 were multiplied by the factor $(1 + 6.7 \times 10^{-8})$. The $A \ ^2\Pi \rightarrow X \ ^2\Sigma^+$ lines were calibrated using several very strong atomic transitions common to both the MgH and MgD spectra. Absolute experimental instrumental uncertainties of 0.005 cm^{-1} were assigned to all of the unblended lines. Further details regarding uncertainties in the data are discussed below.

B. Characterizing the Excited States. Coincidental crossings of energy levels of the $A \ ^2\Pi$ and $B' \ ^2\Sigma^+$ states result in numerous perturbations throughout the spectra. Perturbations were identified by observing the shifts in both the P and R branches of the $B' \ ^2\Sigma^+ \rightarrow X \ ^2\Sigma^+$ bands together with the corresponding opposite-direction shifts in the $A \ ^2\Pi \rightarrow X \ ^2\Sigma^+$ spectra. Unfortunately, including such perturbed lines in the data set precludes the possibility of fitting those excited states to analytic potential energy functions at the present time. Consequently, the present analysis represents all of the observed levels of the $A \ ^2\Pi$ and $B' \ ^2\Sigma^+$ states as independently fitted term values. A full deperturbation analysis of the data for these excited states remains the subject of ongoing work.

Six strong branches were observed in the $A \ ^2\Pi \rightarrow X \ ^2\Sigma^+$ system, consisting of $\Delta J = -1, 0$, and $+1$ (P, Q, and R) branches for both the $A \ ^2\Pi_{1/2}$ and $A \ ^2\Pi_{3/2}$ components. Some satellite branches (e.g., P_{12} and R_{21}) were also observed.

In the $B' \ ^2\Sigma^+ \rightarrow X \ ^2\Sigma^+$ system, multiple off-diagonal bands were observed as a result of favorable Franck–Condon overlap for at least part of the observed range of J values. For almost all of the bands in this system that were observed to moderately high J , doublet e/f splittings caused by the spin–rotation interaction were observed. Because these splittings could not be

resolved for low J values, the blended lines were assigned to both e and f transitions and assigned a larger than “basic” uncertainty.

C. Spectral Assignments. Although several steps were involved in the assignment of the spectral lines, the process was greatly facilitated by the 1978 work of Balfour and Lindgren,²¹ even though their spectrum was of much lower resolution. In particular, their line lists of the $B' \ ^2\Sigma^+ \rightarrow X \ ^2\Sigma^+$ transitions proved to be very helpful for our initial assignment of the strongest bands of that system. A Loomis–Wood program was used to generate our initial line lists.

We used the parameter-fitting program DParFit³⁴ to check our assignments of the $B' \ ^2\Sigma^+ \rightarrow X \ ^2\Sigma^+$ transitions by using band constants to represent the ground state while treating the observed upper-state levels as individual term values. Apart from its usefulness for confirming our assignments, DParFit assisted in the assignment of 31 weaker bands not observed by Balfour and Lindgren²¹ (who reported 23 bands in our range of wavenumbers) by predicting all of the other possible transitions given the term values of the upper state established from a preliminary analysis of the stronger bands. However, a preliminary direct potential fit was required to locate precisely the higher vibrational levels not observed by Balfour and Lindgren. Specifically, the MgD data that had been assigned at the time (extending up to $v'' = 13$) were fitted using the procedure described below in section IV but with the minor magnesium isotopologue data excluded. The resulting potential function was then employed to predict the remaining bound vibrational levels, which turned out to be $v'' = 14, 15$, and 16 . While that initial fit was not optimal, it was sufficiently precise to locate transitions involving the $v'' = 14$ and 15 levels.

Since the ground state had been well-characterized already, the $A \ ^2\Pi$ term values given in ref 17 were used to identify the strong bands in the $A \ ^2\Pi \rightarrow X \ ^2\Sigma^+$ system (i.e., the $0\text{--}0$, $1\text{--}1$, $0\text{--}1$, and $1\text{--}0$ bands). Assignment of the remaining bands with $v' = 0$ and 1 was then straightforward. We did not pursue assignments of the $A \ ^2\Pi \rightarrow X \ ^2\Sigma^+$ bands with $v' = 2$ or 3 , as no new information on the ground $X \ ^2\Sigma^+$ state would thereby have been obtained. However, in the interest of identifying perturbations, assignment of the remaining data will form part of our future deperturbation analysis.

Our spectra also contained several bands due to the isotopologues ^{25}MgD and ^{26}MgD , for which the $B' \ ^2\Sigma^+ \rightarrow X \ ^2\Sigma^+$ transitions were assigned in the manner described above. We also assigned analogous branches for ^{25}MgH and ^{26}MgH that had not previously been reported. We sought only the strongest bands for these minor isotopologues (i.e., those involving $v' = 0$ and 1), since we are concerned here solely with identifying all of the perturbed levels of the major isotopologues, while data for the minor ones serve only to provide information on the BOB correction functions for the magnesium center (see below).

As mentioned above, an uncertainty of 0.005 cm^{-1} was assigned to all of the unblended lines of ^{24}MgD . Lines assigned to unresolved (blended) e/f splittings were given an uncertainty of 0.015 cm^{-1} , while lines that were blended with other unrelated transitions were assigned an uncertainty of 0.05 cm^{-1} . Lines of the latter type were usually identified by inspection when particular data were determined to be outliers in the band-constant fits. Minor isotopologues were given the same treatment; however, since their lines are much weaker, all of the uncertainty values were doubled, so that data for the major magnesium isotopologues were the most heavily

weighted in our direct potential fits. As previously reported,²⁴ the highly precise infrared and microwave data have uncertainties in the range 10^{-3} – 10^{-6} cm^{-1} .

D. The Data Set. The overall data set is summarized in Table 1 and Figure 2, while Table 2 lists the newly observed

Table 1. Summary of the Data Used in the Present Analysis, in Which v'' is the Vibrational Quantum Number of Observed Levels in the $X^2\Sigma^+$ State

isotopologue	v'' range	no. of data	source
Microwave			
²⁴ MgH	0–1	14	ref 24
²⁴ MgD	0–0	9	ref 24
²⁶ MgH	0–0	2	ref 24
Infrared			
²⁴ MgH	0–4	366	ref 24
²⁴ MgD	0–5	389	ref 24
²⁵ MgH	0–3	185	ref 24
²⁵ MgD	0–4	149	ref 24
²⁶ MgH	0–3	179	ref 24
²⁶ MgD	0–4	163	ref 24
Visible			
²⁴ MgH	0–11	7073	ref 29
²⁴ MgD	0–15	7438	this work
²⁵ MgH	3–8	815	this work
²⁵ MgD	4–11	1235	this work
²⁶ MgH	3–8	780	this work
²⁶ MgD	4–11	1306	this work
Total no. of data: 20103			

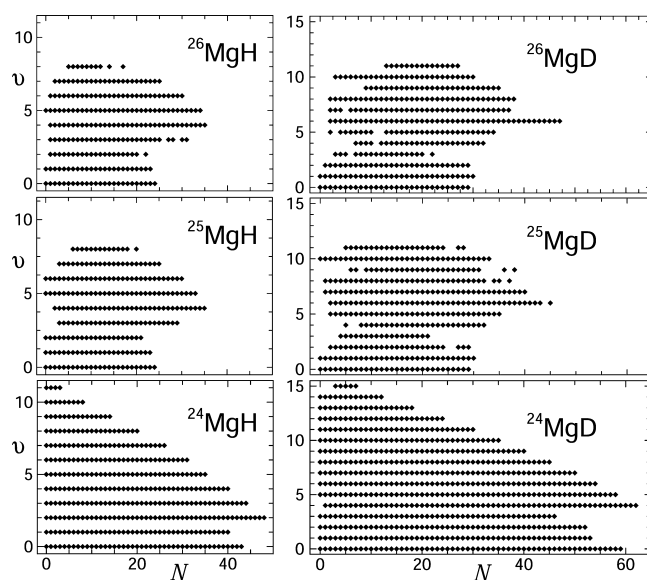


Figure 2. Plot of all of the observed rovibrational levels in the ground state of each isotopologue, showing the extent to which that electronic state has been covered by the data.

bands of ²⁴MgD and provides a qualitative indication of their intensities. For the analysis described below, previously reported microwave and infrared data on the ground $X^2\Sigma^+$ state for all six isotopologues, together with visible transitions from the $B'^2\Sigma^+$ and $A^2\Pi$ states of ²⁴MgH, were combined with new observations of transitions from the $B'^2\Sigma^+$ and $A^2\Pi$ states of ^{24,25,26}MgD and ^{25,26}MgH. The new data set for the $B'^2\Sigma^+ \rightarrow$

Table 2. Observed (v',v'') Bands in the $B'^2\Sigma^+ \rightarrow X^2\Sigma^+$ and $A^2\Pi \rightarrow X^2\Sigma^+$ Systems of ²⁴MgD^a

$A^2\Pi$			$B'^2\Sigma^+$				
$v' = 0$	$v' = 1$	$X^2\Sigma^+$	$v' = 0$	$v' = 1$	$v' = 2$	$v' = 3$	$v' = 4$
vs	s	$v'' = 0$					
s	vs	$v'' = 1$					
s	s	$v'' = 2$				w	
	s	$v'' = 3$			w	w	w
		$v'' = 4$	s	s	s	s	w
		$v'' = 5$	s	s	s	s	w
		$v'' = 6$	s	s	w	w	w
		$v'' = 7$	s	s	s	s	w
		$v'' = 8$	s	s	s	s	w
		$v'' = 9$	s	s	s	w	w
		$v'' = 10$	s	s	w	s	w
		$v'' = 11$	w	s	s	s	w
		$v'' = 12$		w	s	w	w
		$v'' = 13$		w	w	w	w
		$v'' = 14$				w	w
		$v'' = 15$				w	

^aBand intensities are classified as very strong (“vs”), strong (“s”), or weak (“w”).

$X^2\Sigma^+$ system of ²⁴MgD consists of 55 bands involving $v' = 0, 1, 2, 3$, and 4 of the $B'^2\Sigma^+$ state and $v'' = 2$ –15 of the $X^2\Sigma^+$ state, while that for the $A^2\Pi \rightarrow X^2\Sigma^+$ system consists of $\Delta v = 0, \pm 1$, and ± 2 sequence bands originating from $v' = 0$ and 1. Altogether, these 20 103 data span 99.88% of the well depth. This includes the observation of transitions involving several broadened quasi-bound levels, which shows that some vibrational levels are followed almost all the way to their centrifugal barrier maxima, where tunneling predissociation becomes important.

For all of the bound vibrational levels of the ground $X^2\Sigma^+$ state of ²⁴MgD, Table 3 lists the J value, the energy relative to the dissociation asymptote, and (for quasi-bound levels) the predicted tunneling width for the highest observed rotational state. The calculated line widths were generated from the DPF program DPotFit that was used for our data analysis.³⁵ This table also lists, for each v , the J value for what is predicted to be the very highest rotational level lying below the centrifugal barrier maximum for that v .

III. DIRECT-POTENTIAL-FIT DATA ANALYSIS

A. The Radial Hamiltonian. An accurate analytic potential energy function is the best way of summarizing what is known about a molecule in a given electronic state. Such a function should (i) be flexible—able to represent all available data (on average) within the experimental uncertainties; (ii) be “well-behaved”—continuous and differentiable to all orders at all distances; (iii) be robust—able to provide physically reasonable extrapolations outside the region over which the data used to determine the potential are sensitive; (iv) be compact—defined by a minimum number of empirical parameters; and (v) incorporate the correct theoretically known long-range behavior of the molecular state in question.

The best means for determining such a potential function from spectroscopic data is to perform a “direct-potential-fit” (DPF) data analysis, in which simulated spectra generated from a trial analytic potential function are compared with the experimental data and a least-squares fit is employed to optimize the parameters defining that potential. The present

Table 3. Identity, Energy (Relative to the Potential Asymptote), and Width (for Quasi-Bound Levels) of the Highest Observed Rotational State for Each Vibrational Level of the $X^2\Sigma^+$ State of ^{24}MgD and the Rotational Quantum Number $J_{\text{last}}^{\text{pred}}$ for What Is Predicted To Be the Very Highest Quasi-Bound (Lying below the Centrifugal Barrier Maximum) Rotational State for Each v'' (Energies in cm^{-1})

v	highest observed			predicted $J_{\text{last}}^{\text{pred}}$
	$J_{\text{max}}^{\text{obs}}$	$E_{v,N} - \mathcal{D}$	width	
0	58	-1364.20	—	86
1	52	-2144.17	—	81
2	51	-1576.16	—	76
3	45	-2163.98	—	71
4	62	2500.44	0.0012	67
5	58	2114.30	0.0032	62
6	54	1780.06	0.010	58
7	50	1494.01	0.051	53
8	45	1098.83	0.022	48
9	40	7850.04	0.015	43
10	35	546.51	0.022	38
11	30	372.91	0.096	32
12	24	187.19	0.037	26
13	18	77.46	0.030	20
14	12	17.56	0.002	13
15	7	0.44	3.1×10^{-7}	8
16	—	—	—	3

study involves a combined-isotopologue data analysis that simultaneously treats data for the six isotopologues formed by ^{24}Mg , ^{25}Mg , and ^{26}Mg with H and D and takes account of BOB corrections to both the rotationless and centrifugal potentials as well as of $^2\Sigma$ rotational level splittings. We begin by describing the effective radial Hamiltonian used in this work.

As in most DPF data analyses reported to date, the present work uses a form of the effective radial Hamiltonian introduced by Watson, in which BOB terms associated with the radial kinetic energy operator are incorporated into both an effective “adiabatic” correction to the rotationless potential and the nonadiabatic centrifugal BOB correction.^{36,37} Following the convention of ref 38 for mass scaling of the BOB terms and that of Paper 1 for describing the spin–rotation interaction, the effective radial Schrödinger equation for a diatomic molecule A–B in a $^2\Sigma^+$ electronic state is written as

$$\begin{aligned} \hat{H}\psi_{v,N}(r) = & \left\{ -\frac{\hbar^2}{2\mu_\alpha} \frac{d^2}{dr^2} + [V_{\text{ad}}^{(1)}(r) + \Delta V_{\text{ad}}^{(\alpha)}(r)] \right. \\ & + \frac{\hbar^2[N(N+1)]}{2\mu_\alpha r^2} [1 + g^{(\alpha)}(r)] \\ & \left. + s(e/f; N) \Delta V_\Sigma(r) \right\} \psi_{v,N}(r) \\ = & E_{v,N} \psi_{v,N}(r) \end{aligned} \quad (1)$$

in which $V_{\text{ad}}^{(1)}$ is the effective adiabatic internuclear potential for a selected reference isotopologue, $\Delta V_{\text{ad}}^{(\alpha)}(r)$ is the difference between the effective adiabatic potential for isotopologue α and that for reference isotopologue ($\alpha = 1$), μ_α is the usual reduced mass of atoms A and B, and $g^{(\alpha)}(r)$ is the effective nonadiabatic centrifugal-potential correction function for isotopologue α . The potential energy and centrifugal BOB corrections are each

expressed as a sum of contributions associated with the two constituent atoms:^{36–38}

$$\Delta V_{\text{ad}}^{(\alpha)}(r) = \frac{\Delta M_{\text{A}}^{(\alpha)}}{M_{\text{A}}^{(\alpha)}} \tilde{S}_{\text{ad}}^{\text{A}}(r) + \frac{\Delta M_{\text{B}}^{(\alpha)}}{M_{\text{B}}^{(\alpha)}} \tilde{S}_{\text{ad}}^{\text{B}}(r) \quad (2)$$

$$g^{(\alpha)}(r) = \frac{M_{\text{A}}^{(1)}}{M_{\text{A}}^{(\alpha)}} \tilde{R}_{\text{na}}^{\text{A}}(r) + \frac{M_{\text{B}}^{(1)}}{M_{\text{B}}^{(\alpha)}} \tilde{R}_{\text{na}}^{\text{B}}(r) \quad (3)$$

in which $\Delta M_{\text{A}}^{(\alpha)} \equiv M_{\text{A}}^{(\alpha)} - M_{\text{A}}^{(1)}$ is the difference between the mass of atom A in isotopologue α and that in the reference isotopologue and the expressions used for the radial strength functions $\tilde{S}_{\text{ad}}^{\text{A/B}}(r)$ and $\tilde{R}_{\text{na}}^{\text{A/B}}(r)$ are described in section III.C. As in Paper 1, following the approach introduced in ref 39 for Λ -doubling interactions, the rotational level splittings due to the spin–rotation interactions in a molecule with $^2\Sigma^+$ symmetry are taken into account by inclusion of the radial strength function $\Delta V_\Sigma(r)$ with the numerical factors $s(e;N) = +N/2$ for states with e symmetry and $s(f;N) = -(N+1)/2$ for those with f symmetry.⁴⁰

B. The Morse/Long-Range (MLR) Potential Function.

The choice of an optimum potential function form is a central concern in the DPF method. Paper 1 used the “basic” initial form of the (then) recently developed⁴¹ Morse/Long-Range (MLR) potential function to model the rotationless adiabatic internuclear potential of MgH. The version of that function used here incorporates significant extensions of the MLR form introduced in refs 42 and 43. These extensions allow us to obtain more compact (fewer-parameter) potential functions that also have more reasonable physical behavior in the short-range extrapolation region than was obtained using the basic version of the model.⁴³

A central feature of the MLR potential function form is that it incorporates the inverse-power long-range behavior characteristic of all intermolecular interactions, namely,

$$V_{\text{MLR}}(r) \approx \mathcal{D} - \frac{C_{m_1}}{r^{m_1}} - \frac{C_{m_2}}{r^{m_2}} - \dots \quad (4)$$

in which the powers m_i and coefficients C_{m_i} are determined by the nature of the atoms to which the given molecular state dissociates^{44–49} and the leading coefficients may often be computed from theory. Incorporation of the correct long-range behavior is always desirable, but it is particularly important when the observed vibrational levels extend fairly close to the dissociation limit \mathcal{D} . This is the case for MgH and MgD, as their highest observed vibrational levels have outer turning points that lie outside the so-called^{50,51} “Le Roy radius” of 4.7 Å, which is commonly taken to indicate the onset of the region in which the inverse-power sum of eq 4 dominates the interaction.

The updated version of the MLR radial potential energy function used herein takes the form^{42,43,49,52}

$$V_{\text{MLR}}(r) = \mathcal{D}_e \left\{ 1 - \frac{u_{\text{LR}}(r)}{u_{\text{LR}}(r_e)} e^{-\beta(r) y_p^{\text{eq}}(r)} \right\}^2 \quad (5)$$

in which \mathcal{D}_e is the well depth, r_e is the equilibrium internuclear distance, and the explicit radial variable $y_p^{\text{eq}}(r)$ in the exponent is defined as

$$y_p^{\text{eq}}(r) = \frac{r^p - r_e^p}{r^p + r_e^p} \quad (6)$$

The (attractive) long-range tail of the potential function, $u_{\text{LR}}(r)$, is represented by the “damped” inverse-power sum

$$u_{\text{LR}}(r) = \sum_{i=1}^{\text{last}} D_{m_i}(r) \frac{C_{m_i}}{r^{m_i}} \\ = D_{m_1}(r) \frac{C_{m_1}}{r^{m_1}} + D_{m_2}(r) \frac{C_{m_2}}{r^{m_2}} + \dots + D_{m_{\text{last}}}(r) \frac{C_{m_{\text{last}}}}{r^{m_{\text{last}}}} \quad (7)$$

Recent work⁴² has shown that the exponent coefficient function

$$\beta(r) = \beta_{p,q}^{\text{ref}}(r) = y_p^{\text{ref}}(r) \beta_{\infty} + [1 - y_p^{\text{ref}}(r)] \sum_{i=0}^{N_{\beta}} \beta y_q^{\text{ref}}(r)^i \quad (8)$$

is best defined in terms of two radial variables that are similar in form to $y_p^{\text{eq}}(r)$ but involve the use of a different expansion center, $r_{\text{ref}} > r_e$, and separate integer powers p and q , one of which is the same as that appearing in eq 6:

$$y_p^{\text{ref}}(r) = \frac{r^p - r_{\text{ref}}^p}{r^p + r_{\text{ref}}^p}, \quad y_q^{\text{ref}}(r) = \frac{r^q - r_{\text{ref}}^q}{r^q + r_{\text{ref}}^q} \quad (9)$$

A central property of the MLR form is the fact that the limiting asymptotic value $\beta_{\infty} \equiv \lim_{r \rightarrow \infty} \beta(r)$ of the exponent coefficient function of eq 8 is

$$\beta_{\infty} \equiv \ln\{2\mathcal{D}_e/u_{\text{LR}}(r_e)\} \quad (10)$$

This means that for $p > (m_{\text{last}} - m_1)$ (see below), $V_{\text{MLR}}(r)$ behaves asymptotically as

$$V_{\text{MLR}}(r) \approx \mathcal{D}_e - u_{\text{LR}}(r) + O\left\{\frac{u_{\text{LR}}(r)^2}{4\mathcal{D}_e}\right\} \quad (11)$$

For cases in which m_1 is relatively small, the nature of the last term in eq 11 sometimes requires additional constraints to be introduced.^{42,52} However, in the present application $m_1 = 6$, and such constraints are not required.

It should be noted that the power p in eqs 5, 6, and 8 must be larger than the difference between the (inverse) powers of the first and last terms included in eq 7 to prevent the long-range behavior of the exponential term in eq 5 from interfering with the long-range behavior specified by eq 7.^{41,42} However, this restriction often requires p to be fairly large (e.g., $p \geq 5$ in the present work), which in turn causes $y_p(r)$ to be relatively flat (and close to its limits of ± 1) over a significant fraction of the data-sensitive range of r . This “stiff” behavior of the expansion variable tends to make it difficult to converge on an accurate potential function model without introducing an undesirably large number of exponent polynomial expansion coefficients.

The difficulty encountered in dealing with the large values of p required by the restriction that $p > (m_{\text{last}} - m_1)$ led to the introduction of the additional radial variable $y_q(r)$ of eqs 8 and 9.⁴² The form of these expressions means that the value assigned to the power q has no effect on the long-range behavior of the exponential term in eq 5, so assigning q a relatively small value (say $q = 2-4$) enables the determination of accurate potential functions having smaller exponent polynomial orders N than would otherwise be required.⁵³ The introduction of a radial variable expansion center r_{ref} ($> r_e$) that lies close to the geometric mean of the inner and outer ends of the range of r to which the data are sensitive also helps to reduce the order of the (exponent) polynomial expansion required to obtain a given quality of fit. It is also noteworthy

that the introduction of $r_{\text{ref}} > r_e$ also leads to expansion coefficients β_i whose magnitudes are more commensurate with the domain of the variable and the range of the function than is the case for $r_{\text{ref}} = r_e$.⁴³ The impact of these two extensions of the basic MLR model of ref 41 is demonstrated by the fact that the exponent coefficient function of the MLR potential obtained in the present work contains six fewer exponent polynomial expansion parameters (almost one-third fewer!) than were required in the fit to the ²⁴MgH data alone in Paper 1.²⁹

Finally, we note that although all intermolecular potential energy functions eventually take on the simple inverse-power form of eq 4 at very long range,⁴⁴⁻⁴⁶ it has long been known that at shorter “molecular” distances, overlap of the electron distributions of the interacting atoms weakens the inverse-power dispersion terms and removes their high-order singular behavior as $r \rightarrow 0$.⁵⁴ This was the reason for the introduction of the “damping functions” $D_{m_i}(r)$ in eq 7. However, as discussed in ref 43, the use of an appropriate damping function form not only improves the physical behavior of MLR potential functions at long range but also substantially improves their extrapolation behavior at small distances. As a result, following the recommendation of ref 43, the damping functions appearing in our MLR model for the potential energy function of MgH are the $s = -1$ versions of the generalized Douketis-type functions⁵⁵

$$D_m^{(s)} = \left\{ 1 - \exp\left[-\frac{b^{(s)}(\rho r)}{m} - \frac{c^{(s)}(\rho r)^2}{m^{12}}\right] \right\}^{m+s} \quad (12)$$

A key property of this generalized⁴³ damping function form is the fact that for all m ,

$$\lim_{r \rightarrow 0} \left\{ \frac{D_m^{(s)}(r)}{r^m} \right\} \propto r^s \quad (13)$$

Within the MLR potential function form, this causes the potential energy function to behave as r^{2s} at very short range. The two system-independent parameters in these $s = -1$ damping functions have values $b^{(-1)} = 3.30$ and $c^{(-1)} = 0.423$.⁴³

Within the damping function form of eq 12, the constant ρ is a system-dependent range parameter introduced to take account of the sizes of the electron clouds on the interacting atoms. Following Douketis et al.,⁵⁵ for interacting atoms A and B we write

$$\rho \equiv \rho_{\text{AB}} = \frac{2\rho_A\rho_B}{\rho_A + \rho_B} \quad (14)$$

in which $\rho_A = (\text{IP}^{\text{A}}/\text{IP}^{\text{H}})^{2/3}$ is defined by the ratio of the ionization potential of atom A, IP^{A} , and that of a ground-state H atom, IP^{H} . The value of this dimensionless parameter used to define the damping functions employed in the present model for ground-state MgH is $\rho_{\text{MgH}} = 0.81$.

C. Born–Oppenheimer Breakdown Radial Strength Functions. The empirical determination of radial functions to characterize the nature and strength of BOB contributions to the radial Hamiltonian was pioneered by J. A. Coxon over a quarter century ago^{56,57} and has evolved to become an almost routine part of diatomic DPF data analyses for both hydride⁵⁸⁻⁶² and non-hydride^{39,42,52,63,64} systems. The present work follows the approach introduced in ref 65, in which the radial strength functions defining the adiabatic and centrifugal

BOB functions are written in the same form used for the MLR exponent coefficient function, specifically,

$$\tilde{S}_{\text{ad}}^{\text{A,B}}(r) = u_{\infty}^{\text{A,B}} y_{p_{\text{ad}}}^{\text{eq}}(r) + [1 - y_{p_{\text{ad}}}^{\text{eq}}(r)] \sum_{i=0}^{N_{\text{ad}}^{\text{A,B}}} u_i y_{q_{\text{ad}}}^{\text{eq}}(r)^i \quad (15)$$

$$\tilde{R}_{\text{na}}^{\text{A,B}}(r) = t_{\infty}^{\text{A,B}} y_{p_{\text{na}}}^{\text{eq}}(r) + [1 - y_{p_{\text{na}}}^{\text{eq}}(r)] \sum_{i=0}^{N_{\text{na}}^{\text{A,B}}} t_i y_{q_{\text{na}}}^{\text{eq}}(r)^i \quad (16)$$

in which $p_{\text{ad}} = m_1 = 6$ is the (inverse) power associated with the leading contribution to $u_{\text{LR}}(r)$. Our adoption of the convention that the absolute zero of energy be defined as the energy of the ground-state atoms at infinite separation⁶⁵ means that for all electronic states that dissociate to ground-state atoms, $u_{\infty}^{\text{A}} = u_{\infty}^{\text{B}} = 0$. In contrast, for an electronic state that dissociates to yield an electronically excited atom A^* , the value of u_{∞}^{A} would be defined by the isotope shift of the atomic $\text{A} \rightarrow \text{A}^*$ transition energy.⁶⁵ However, since the present work uses a potential energy function model only for the ground $X^2\Sigma^+$ state of MgH , this question does not arise here. The factors $t_{\infty}^{\text{A,B}}$ similarly define the limiting asymptotic values of the nonadiabatic centrifugal BOB functions $\tilde{R}_{\text{na}}^{\text{A,B}}(r)$, but the arguments presented in ref 65 indicate that except for cases in which the electronic state dissociates to yield an atomic ion (A^+), $t_{\infty}^{\text{A}} = 0$. Finally, in view of Watson's conclusion that the value of $\tilde{R}_{\text{na}}^{\text{A,B}}(r = r_e)$ cannot be determined from transition-energy data alone,^{36,37} we therefore fix $t_0^{\text{H}} = t_0^{\text{Mg}} = 0$.

As discussed in ref 65, the integer p_{ad} in eq 15 must be set at $p_{\text{ad}} = m_1$, the power of the leading term in eq 7, in order to ensure that the long-range tail of the potential energy function has the same limiting inverse-power behavior for all isotopologues of a given species. However, there are no analogous restrictions on the value of q_{ad} . Similarly, the value of q_{na} does not affect the limiting long-range behavior of $\tilde{R}_{\text{na}}^{\text{A,B}}(r)$, and since we know of no constraint on the limiting long-range behavior of the latter function, it is convenient to fix $q_{\text{na}} = p_{\text{na}}$.

We know of no theoretical predictions regarding the characteristic limiting long-range behavior expected for the Σ -doubling radial strength function $\Delta V_{\Sigma}^{(\alpha)}$. Hence, it is convenient to represent it using a simple polynomial expansion in the reduced variable $y_{q_{\Sigma}}^{\text{eq}}(r)$ of eq 6:

$$\Delta V_{\Sigma}^{(\alpha)}(r) = \frac{\hbar^2}{2\mu_{\alpha} r^2} \sum_{i=0}^{N_{\Sigma}} w_i^{\Sigma} y_{q_{\Sigma}}^{\text{eq}}(r)^i \quad (17)$$

As for the expansions in eqs 15 and 16, there are no theoretical constraints on the choice of the integer q_{Σ} .

D. Aspects of the Fitting Procedure. As in any DPF procedure, for a given assumed model of the potential energy function(s) and any associated BOB functions, eq 1 is solved numerically to yield the eigenvalues $E_{v,N}$ and eigenfunctions $\psi_{v,N}(r)$ for the upper and lower levels of every observed transition. The difference between the eigenvalues for those upper and lower levels yields an estimate of the transition energy for comparison with experiment, and use of the Hellmann–Feynman theorem

$$\frac{\partial E_{v,N}}{\partial p_j} = \left\langle \psi_{v,N}(r) \left| \frac{\partial \hat{H}}{\partial p_j} \right| \psi_{v,N}(r) \right\rangle \quad (18)$$

yields the partial derivatives required for performing a least-squares fit to optimize the parameters p_j defining the

parametrized potential energy and BOB functions. The DPF data analysis described below was performed using the computer program DPotFit,³⁵ within which all of the requisite eigenvalue calculations were performed using a Numerov propagation algorithm⁶⁶ on the radial range $r \in [0.6, 99] \text{ \AA}$ with a radial mesh of 0.0025 \AA .

The overall quality of fit of a given model to a set of N data points is represented here by the dimensionless root-mean-square deviation

$$\overline{dd} \equiv \sqrt{\frac{1}{N} \sum_{i=1}^N \left(\frac{y_i^{\text{calc}} - y_i^{\text{obs}}}{u_i} \right)^2} \quad (19)$$

in which y_i^{calc} and y_i^{obs} are, respectively, the calculated and observed values of the i th datum, while u_i is its estimated experimental uncertainty. A value of $\overline{dd} \lesssim 1$ indicates that on average the model explains all of the input data within their estimated uncertainties. It should also be noted that obtaining values of \overline{dd} that are significantly smaller than unity often indicates that the estimated experimental uncertainties were unduly pessimistic.

As stated earlier, the extensive perturbations in the excited electronic states led us to treat all of their observed levels as independent term values. As a result, our final global fits involved a total of 2433 fitting parameters, of which 51 were associated with the Hamiltonian for the ground $X^2\Sigma^+$ state while the remaining 2382 were those fitted term values. Of the latter, some 115 (4.8%) were for levels that were accessed by only a single emitted line. These 115 data of course contain no information about the ground electronic state, and in principle they should have been excluded from the sum in eq 19 since all of the associated $y_i^{\text{calc}} - y_i^{\text{obs}}$ values are identically zero. However, we left them in because of the residual information they contain about the excited-state levels, but we corrected the final value of \overline{dd} to take account of this.

Since the eigenvalues $E_{v,N}$ of the ground $X^2\Sigma^+$ state are not linear functions of the parameters defining the effective radial Hamiltonian \hat{H} , a realistic initial set of trial parameters is required to initiate the fitting cycle. Such trial parameters may be generated from a fit of the chosen potential form to a mesh of approximate potential function points, which in turn may be obtained from ab initio calculations or from the application of the semiclassical Rydberg–Klein–Rees inversion procedure⁶⁷ to the results of a preliminary Dunham-type analysis. In the present case, we selected a grid of points generated from the fitted potential reported in Paper 1 and used the program betaFIT⁶⁸ to generate the required sets of trial potential function parameters. Because the BOB and Σ -doubling correction functions are relatively weak, initial trial parameter values of zero sufficed for them.

IV. RESULTS: NEW POTENTIAL ENERGY AND BOB FUNCTIONS FOR THE GROUND STATE OF MGH

A. New Potential Energy and BOB Functions for the Ground State of MgH. Determining an optimum radial Hamiltonian description of the ground state of MgH is a complicated multidimensional problem because it is necessary to determine optimum descriptions of six different radial functions: (i) the exponent coefficient function $\beta(r)$ of the MLR potential; (ii) and (iii) the potential energy and centrifugal BOB functions for the H-atom terms in eqs 2 and 3; (iv) and (v) the analogous potential energy and BOB

functions for the Mg atom; and (vi) the $^2\Sigma$ -doubling radial strength function $\Delta V_{\Sigma}^{(a)}(r)$. Fortunately, isotope effects and the results of Paper 1 simplify the problem considerably. In particular, if we initially consider only the one isotopologue for which the data are most extensive, ^{24}MgH , we need consider only $\beta(r)$, the H-atom centrifugal BOB function $\tilde{R}_{\text{na}}^{\text{H}}(r)$, and the $^2\Sigma$ -doubling radial strength function $\Delta V_{\Sigma}^{(a)}(r)$. Although the Mg-atom centrifugal BOB function $\tilde{R}_{\text{na}}^{\text{Mg}}(r)$ may also affect those data, the relative atomic mass ratio of 24:1 leads us to expect that its effect will be relatively small, allowing it to be ignored initially.

Throughout the present work, the long-range tail of the MLR potential was represented by a three-term version of eq 7 with $m_i = 6, 8$ and 10; the corresponding coefficients C_{m_i} were fixed at the theoretical values of Mitroy and Zhang,⁶⁹ and the damping functions were represented by the $s = -1$ versions of the generalized Douketis-type functions of eq 12. Because of the particular inverse powers appearing in our long-range tail function $u_{\text{LR}}(r)$ (6, 8, and 10), the power p defining the dimensionless radial variables of eqs 6 and 9 must be >4 , and throughout most of the present work it was fixed at $p = 5$. The remaining problem was to determine optimum values for the exponent polynomial order N_{β} , the power q defining the expansion variable of eqs 8 and 9, and the expansion center r_{ref} of eq 9. A realistic preliminary estimate of this last quantity is the geometric mean of the inner and outer turning points for the highest vibrational level included in the analysis,⁴³ which in the present case suggested $r_{\text{ref}} \approx 2.9$ Å. For any given $\{N_{\beta}, p, q, r_{\text{ref}}\}$ model, it is also necessary to have realistic initial trial values of the exponent coefficients $\{\beta_i\}$ to begin the nonlinear fit to the experimental data. They were obtained by the procedure described at the end of section III.D.

Some preliminary experimentation indicated that polynomials of order $N_{\text{na}}^{\text{H}} \approx 7$ with $p_{\text{na}}^{\text{H}} = q_{\text{na}}^{\text{H}} = 4$ and $N_{\Sigma} \approx 3$ with $q_{\Sigma} = 4$ should describe the centrifugal BOB and $^2\Sigma$ -doubling correction functions properly, so these models were assumed for those two functions in our initial work on determining optimum values of N_{β} , r_{ref} , and q . Fits were then performed across a range of r_{ref} values for a selection of combinations of N_{β} and q , yielding the results presented in Figure 3. The three plots for fits performed using the $q = 4$ expansion variables (red curves joining red squares) illustrate two general results: (i) for any given combination of q and r_{ref} a fit of optimum quality (i.e., minimum \overline{dd}) can always be obtained if N_{β} is made sufficiently large; and (ii) the range of r_{ref} values yielding a good

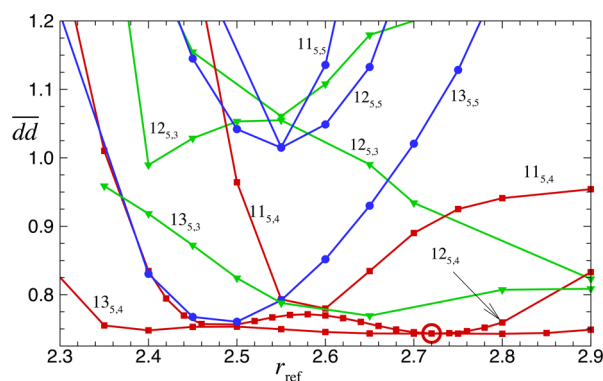


Figure 3. Quality of fit to the 7453 ^{24}MgH data for MLR models $N_{p,q}$ as functions of r_{ref} where $N \equiv N_{\beta}$.

quality of fit becomes ever wider as N_{β} increases. On the basis of the results shown here, we chose $N_{\beta} = 12$, $r_{\text{ref}} = 2.72$ Å, and $q = 4$ to define our recommended MLR potential for MgH . This model requires six fewer fitted exponent expansion parameters β_i than did the recommended model of Paper 1.²⁹ This compactness was achieved because of the additional sophistication introduced into the model by including the expansion center r_{ref} and expansion variable power q as additional parameters and because of the improvements in the short-range behavior arising from the introduction of damping functions into our definition of $u_{\text{LR}}(r)$.⁴³

Given a recommended model for the potential energy function, it is appropriate to test the convergence of the fit with respect to the orders of the polynomial functions used to represent the H-atom centrifugal BOB correction and the $^2\Sigma$ -splitting radial strength functions. These results are summarized in Figure 4, where we see that convergence is achieved at $N_{\text{na}}^{\text{H}} =$

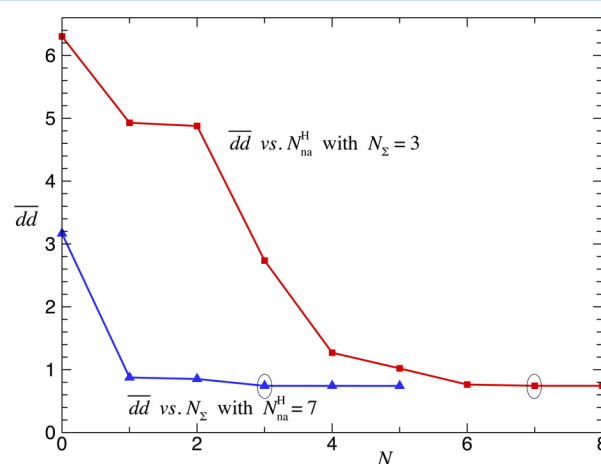


Figure 4. Convergence of the fits to the 7453 ^{24}MgH data with respect to the orders of the polynomials used to represent the H-atom centrifugal BOB function $\tilde{R}_{\text{na}}^{\text{H}}(r)$ and the $^2\Sigma$ -doubling strength function $\Delta V_{\Sigma}^{(1)}(r)$. These results were all obtained using the optimum $N_{p,q} = 12_{5,4}^{2,72}$ MLR model implied by the results in Figure 3.

7 and $N_{\Sigma} = 3$. Tests showed that expanding these functions in terms of radial variables defined by $p_{\text{na}}^{\text{H}} = p_{\Sigma} = 3$ (rather than 4) did not affect this convergence behavior. Figure 5 shows the nature of the radial strength functions determined in this way. It should be noted that the short-range divergence of the $\tilde{R}_{\text{na}}^{\text{H}}(r)$ functions occurs at very small distances, well outside the data-sensitive region. Moreover, although it appears that the radial function $\Delta V_{\Sigma}^{(1)}(r)$ for $N_{\Sigma} = 3$ has not fully converged to that for $N_{\Sigma} = 4$, the values of \overline{dd} for those two cases differ by only 0.1%, a difference deemed to be too small to justify the inclusion of yet another parameter in the model. The width of the “data region” in the top panel of Figure 5 is defined by the inner and outer turning points of the highest vibrational level for which $^2\Sigma$ splittings were resolved, while that for the H-atom centrifugal BOB function is defined by the turning points of the highest observed vibrational level of ^{24}MgH .

Our next objective was to incorporate data for the minor Mg isotopologues into the analysis and to determine the associated BOB correction functions. As shown in Table 1, the vibrational range spanned by these data is distinctly smaller than that associated with the dominant isotopologue, so we anticipated that relatively few terms would be required to define these functions. The inset and the blue circles in Figure 6 show that

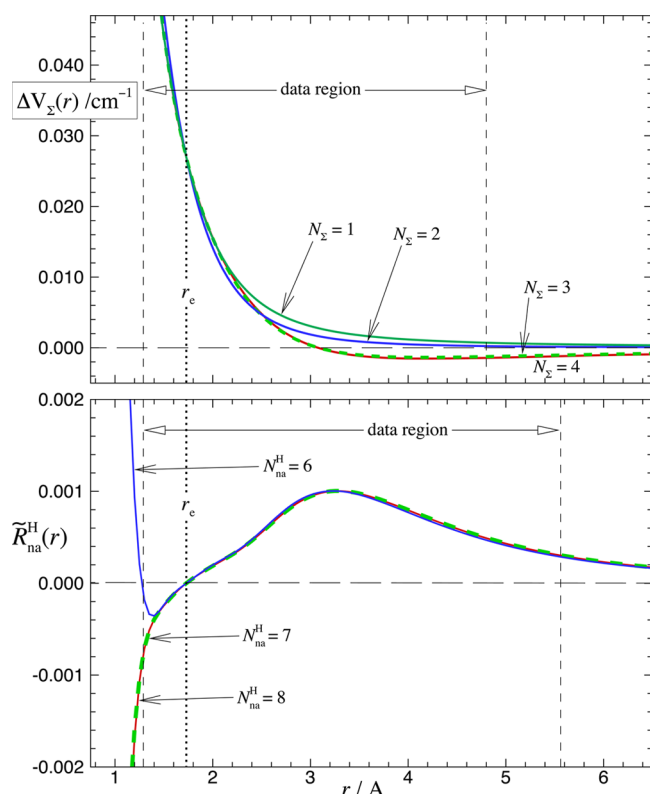


Figure 5. Plots of (bottom) the H-atom centrifugal BOB function $\tilde{R}_{na}^H(r)$ and (top) the 2Σ -doubling radial strength function $\Delta V_{\Sigma}^{(1)}(r)$ determined in this analysis, showing the convergence of these functions with increasing polynomial orders N_{na}^H and N_{Σ} .

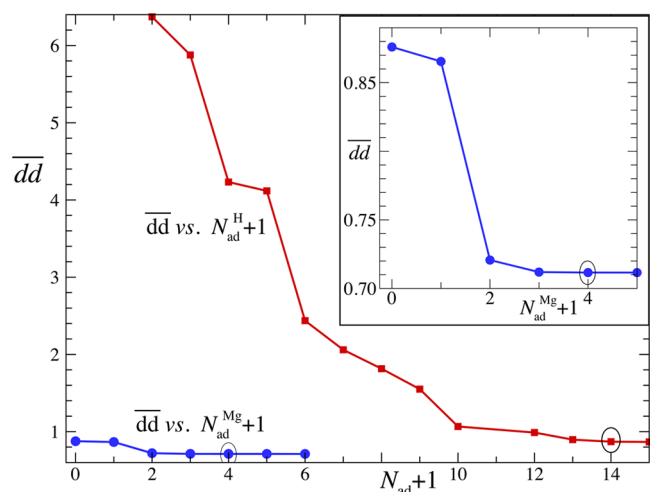


Figure 6. Convergence of fits to all 20 103 MgH and MgD data with respect to the number of terms in the polynomial used to represent the “adiabatic” H-atom potential energy BOB function $\tilde{S}_{ad}^H(r)$ (red squares). The inset and blue circles show the convergence of fits to all 9414 MgH data with respect to the number of fitted coefficients in the polynomial used to represent the “adiabatic” Mg-atom potential energy BOB function $\tilde{S}_{ad}^{Mg}(r)$. All of these results were obtained using the optimum $N_{pd}^{ref} = 12_{5,4}^{2,72}$ MLR model implied by the results in Figure 3 and the centrifugal BOB and 2Σ -splitting functions determined from Figure 4.

convergence with respect to the order of the expansion for the “adiabatic” Mg-atom potential energy BOB correction function occurs at $N_{ad}^{Mg} = 3$. Figure 7 presents plots of the resulting

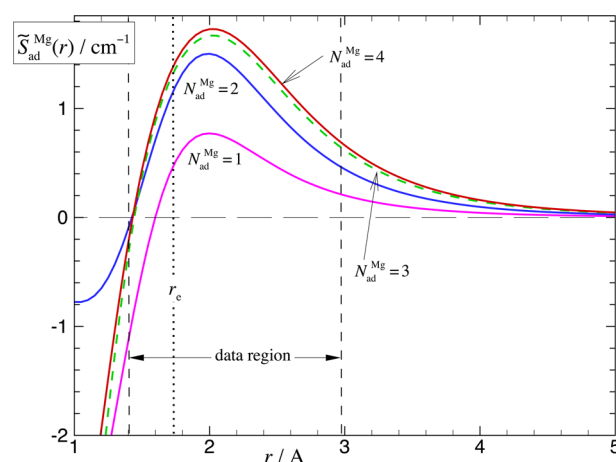


Figure 7. Plots of the fitted Mg-atom adiabatic potential energy BOB functions for increasing values of the polynomial order N_{ad}^{Mg} .

$\tilde{S}_{ad}^{Mg}(r)$ functions for a range of N_{ad}^{Mg} values. While the function for $N_{ad}^{Mg} = 3$ does not appear to be fully converged to that for $N_{ad}^{Mg} = 4$, the values of \overline{dd} for these two cases differ by only 0.004%, and this small difference also did not justify including yet another fitting parameter in the model. The fits were unable to discern any dependence on the Mg-atom centrifugal BOB correction function $\tilde{R}_{na}^{Mg}(r)$.

The next step in our analysis was to determine the adiabatic BOB potential energy correction function $\tilde{S}_{ad}^H(r)$ that would allow not only a unified treatment of the MgH and MgD data but also reliable predictions for MgT transitions. The red squares in Figure 6 show the convergence of fits to all 20 103 MgH and MgD data with respect to the number of nonzero terms in our expression for $\tilde{S}_{ad}^H(r)$. The circle around the result for $N_{ad}^H = 13$ indicates that that is where convergence is achieved. Figure 8 then shows plots of the resulting adiabatic

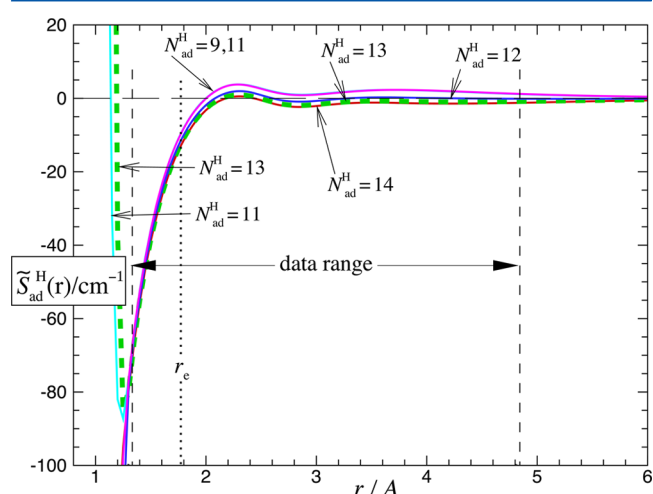


Figure 8. Plots of the fitted H-atom adiabatic potential energy BOB functions for increasing values of the polynomial order N_{ad}^H .

correction functions. Once again, the implausible divergence of these functions only occurs at very short distances, well outside the data-sensitive region.

Finally, it was appropriate to re-examine our determination of the optimum MLR potential function model using fits to all 20 103 MgH and MgD data in place of the 7453 ^{24}MgH data used in the fits summarized in Figure 3. For the four families of

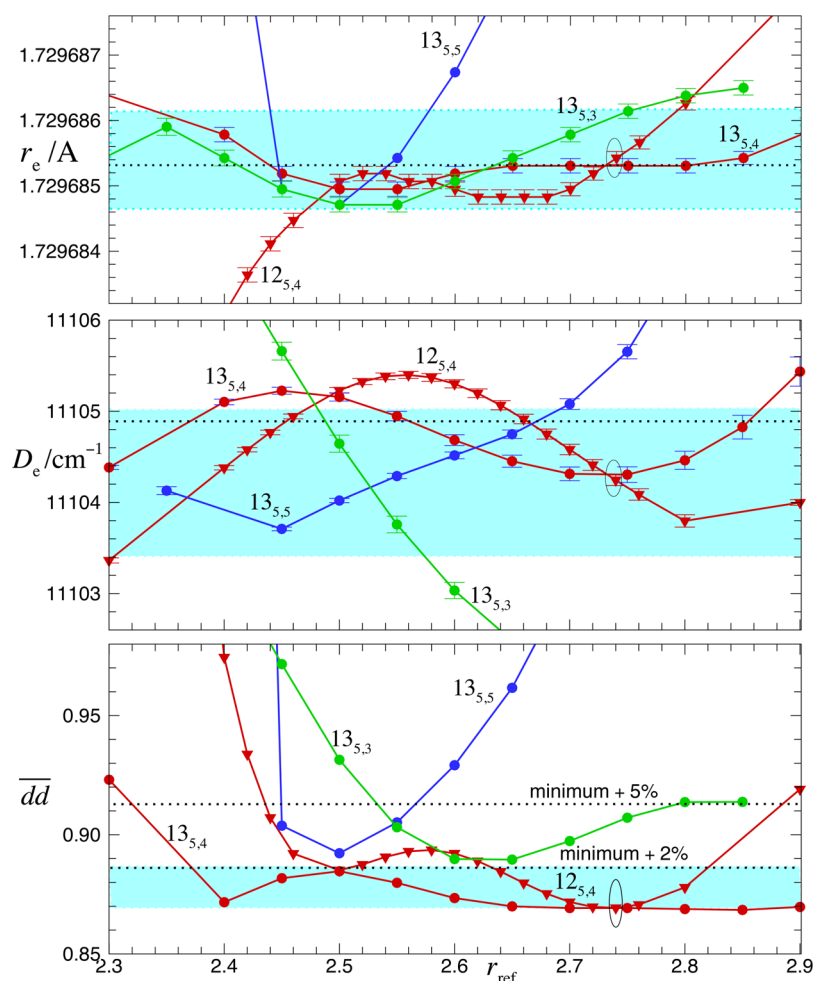


Figure 9. (bottom) Quality of fit of the 20 103 MgH and MgD data to MLR $N_{p,q}$ model potentials as functions of r_{ref} where $N = N_{\beta}$. The shaded region encompasses the models used to estimate the uncertainty due to model dependence, and the circle indicates the recommended model. (middle, top) Fitted values of D_e and r_e for a range of MLR $N_{p,q}$ potential models. The shaded areas indicate the overall estimated parameter uncertainties, while the circles indicate the recommended model.

potential function models that yielded the best results in Figure 3, Figure 9 shows how the global quality of fit and the fitted values of D_e and r_e vary with r_{ref} . From the $d\bar{d}$ values shown in the bottom panel of Figure 9 we conclude that our optimum MLR model remains $N_{p,q} = 12_{5,4}$ but that the optimum value for r_{ref} should be shifted from 2.72 to 2.74 Å.

The algebraic structure of eq 5 ensures that our fitted potential energy function assumes the long-range form $V(r) \approx \mathcal{D} - C_6/r^6 - C_8/r^8 + \dots$ in the limit $r \rightarrow \infty$. This means that as $1/r^2 \rightarrow 0$, a plot of $C_6^{\text{eff}}(r) \equiv r^6[\mathcal{D} - V(r)]$ versus $1/r^2$ should linearly approach a limiting value of C_6^{theory} with a slope of C_8^{theory} . However, one sometimes encounters significant deviations from a monotonic approach to this behavior at distances outside the data-sensitive region (i.e., past the outer turning point of the highest observed level). As a test of this concern, Figure 10 presents plots of this type for five of the “best-fit” models determined from the minima of $d\bar{d}$ in Figures 3 and 9. In the two lower panels of Figure 10 we see that all of these potential function models do indeed have the expected limiting behavior. However, as is often the case for models with relatively low q values, the $13_{5,3}^{2,65}$ model has a spurious extremum between the end of the data region (indicated by the outer turning point for $\nu = 11$) and the asymptotic limit. This unphysical extrapolation behavior confirms that $q = 3$ should

not be used to define the MLR exponent expansion variable for this system. All of the other models show the positive curvature away from the limiting slope that is expected because the third term in $u_{\text{LR}}(r)$ is an attractive C_{10}/r^{10} term. On the basis of this physically sensible extrapolation behavior, and because it requires fewer exponent polynomial expansion coefficients than the other “good” models, we choose the $N_{p,q}^{\text{ref}} = 12_{5,4}^{2,74}$ MLR function as the recommended potential energy function for the ground state of MgH. Figure 11 shows the nature of the exponent coefficient function for this MLR potential.

The parameters defining our final recommended Hamiltonian model for the multi-isotopologue MgH/MgD system are listed in Table 4. A Fortran subroutine for generating the effective potential energy and the centrifugal potential function for any of the isotopologues of MgH is included in the Supporting Information. The uncertainties in D_e and r_e given in Table 4 are the “averaged-over-models” results described below, and analogous model-averaged uncertainties are given for the leading adiabatic BOB parameter for each atom, u_0^{H} and u_0^{Mg} , since they provide a direct measure of the difference between the well depth for isotopologue α and that for the reference isotopologue ($\alpha = 1$):

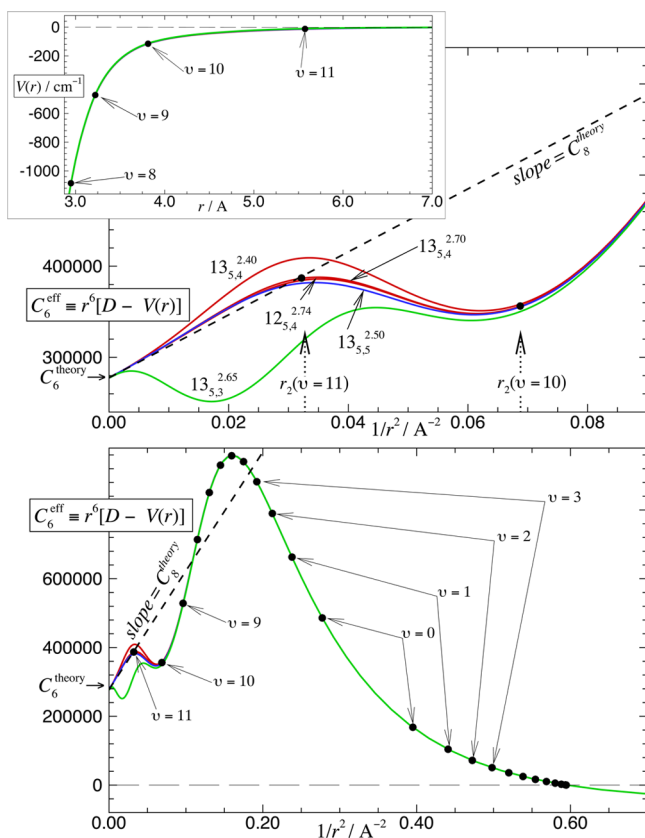


Figure 10. (bottom and middle) Plots of $C_6^{\text{eff}}(r) \text{ cm}^{-1} \text{ \AA}^6$ to test the extrapolation behavior of five of the “best-fit” models of Figure 9. The black points show the positions of the inner and outer turning points of the observed levels of ^{24}MgH . (middle) Expanded version of this $C_6^{\text{eff}}(r)$ plot in the region $1/r^2 < 0.09$ where the $C_6^{\text{eff}}(r)$ plots dip below the limiting C_6/C_8 line. (upper) Plot of these actual potential functions (superimposed in this scale) at distances from the outer turning points for $\nu = 8$ to beyond that for $\nu = 11$.

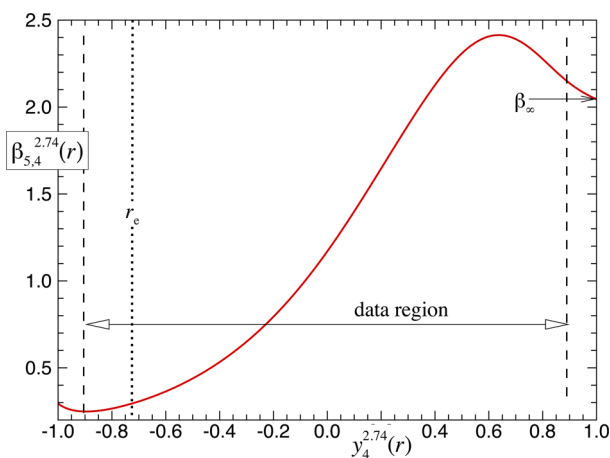


Figure 11. Plot of $\beta(y_4^{2.74}(r))$ showing the range of $y_4(r)$ defined by the turning points of the highest observed vibrational level, $\nu = 11$ of MgH .

$$\delta \mathcal{D}_e^{(\alpha)} = \mathcal{D}_e^{(\alpha)} - \mathcal{D}_e^{(1)} = -\frac{\Delta M_{\text{H}}^{(\alpha)}}{M_{\text{H}}^{(\alpha)}} u_0^{\text{H}} - \frac{\Delta M_{\text{Mg}}^{(\alpha)}}{M_{\text{Mg}}^{(\alpha)}} u_0^{\text{Mg}} \quad (20)$$

However, uncertainties are not listed for the nonphysical parameters characterizing the shapes of the various radial

Table 4. Fitted Parameters Defining the Recommended Radial Hamiltonian for the Isotopologues of MgH in its Ground $X^2\Sigma^+$ State^a

\mathcal{D}_e	11 104.25 \pm 0.80	$\{p_{\text{ad}}, q_{\text{ad}}\}$	$\{6, 4\}$
r_e	1.729 685 4 \pm 0.000 000 7	u_0^{H}	−15.183 \pm 0.61
$\{p, q\}$	$\{5, 4\}$	u_1^{H}	37.524
r_{ref}	2.74	u_2^{H}	−11.607
β_0	1.170 475 46	u_3^{H}	32.2
β_1	1.080 157 9	u_4^{H}	60.57
β_2	2.673 297 1	u_5^{H}	229.5
β_3	2.483 59	u_6^{H}	−1561
β_4	0.740 13	u_7^{H}	−2013
β_5	0.191 47	u_8^{H}	12 530
β_6	0.603 83	u_9^{H}	5360
β_7	−2.4873	u_{10}^{H}	−49 740
β_8	−7.6653	u_{11}^{H}	10 500
β_9	−5.731	u_{12}^{H}	71 100
β_{10}	2.839	u_{13}^{H}	−47 000
β_{11}	6.054	u_{∞}^{H}	[0.0]
β_{12}	2.4		
		u_0^{Mg}	1.31 \pm 0.16
$\{p_{\text{nar}}, q_{\text{na}}\}$	$\{4, 4\}$	u_1^{Mg}	4.18
t_0^{H}	[0.0]	u_2^{Mg}	2.67
t_1^{H}	0.000 726 6	u_3^{Mg}	4
t_2^{H}	0.000 27	u_{∞}^{Mg}	[0.0]
t_3^{H}	0.000 911		
t_4^{H}	0.002 97	$\{q_{\Sigma}\}$	$\{4\}$
t_5^{H}	−0.0019	w_0^{Σ}	0.004 619 3
t_6^{H}	−0.0072	w_1^{Σ}	−0.003 14
t_7^{H}	0.023	w_2^{Σ}	0.000 27
t_{∞}^{H}	[0.0]	w_3^{Σ}	−0.004 54

^aThe $\text{MLR}_{p=5, q=4}^{r_{\text{ref}}=2.74}(N_{\beta}=12)$ potential function incorporates a three-term $u_{\text{LR}}(r)$ function defined by⁶⁹ $C_6 = 2.7755 \times 10^5 \text{ cm}^{-1} \text{ \AA}^6$, $C_8 = 3.4549 \times 10^6 \text{ cm}^{-1} \text{ \AA}^8$, and $C_{10} = 4.6140 \times 10^7 \text{ cm}^{-1} \text{ \AA}^{10}$ and the damping functions of eq 12 with $s = -1$ and $\rho_{\text{AB}} = 0.81$. It should be noted that all of the $\mu_i^{\text{H/Mg}}$ parameters have units of cm^{-1} . This model reproduces the 20 103 observations (on average) to within 0.869 times their estimated experimental uncertainties.

functions. The differences in the well depths for the minor isotopologues implied by eq 20 are listed in Table 5. It should

Table 5. Well-Depth Differences $\Delta \mathcal{D}_e$ and Ground-State Dissociation Energies \mathcal{D}_0 for Nine Isotopologues of MgH

species	$\Delta \mathcal{D}_e / \text{cm}^{-1}$	$\mathcal{D}_0 / \text{cm}^{-1}$
^{24}MgH	0.0	10365.141
^{25}MgH	−0.052(6)	10365.680
^{26}MgH	−0.101(11)	10366.176
^{24}MgD	7.586(30)	10576.971
^{25}MgD	7.533(31)	10577.744
^{26}MgD	7.483(32)	10578.455
^{24}MgT	10.110(41)	10668.371
^{25}MgT	10.057(41)	10669.311
^{26}MgT	10.009(42)	10670.178

be noted, however, that to generate an accurate potential energy function for one of these species, it does not suffice to simply replace the value of \mathcal{D}_e in Table 4 by one obtained using Table 5; rather, one must add the appropriate adiabatic correction function $\Delta V_{\text{ad}}^{(\alpha)}(r)$ of eq 2 to the MLR potential for

the reference isotopologue $^{24}\text{Mg}^1\text{H}$ defined by the parameters of Table 4.

The two upper panels of Figure 9 show that model dependence is a much larger source of uncertainty than are the correlated parameter uncertainties associated with any given fit (error bars on points). To take account of this, the scheme for averaging over models introduced in ref 70 was applied to all of the models whose \overline{dd} values lay within 2% of the lowest value attained (shaded region in the bottom panel of Figure 9). In particular, the statistical weight for parameter value P_i yielded by a particular fit is defined in terms of the correlated 95% confidence limit uncertainty in the value of that parameter yielded by the fit, $u(P_i)$, and the overall quality-of-fit parameter \overline{dd}_i :

$$w_i = \frac{1}{[u(P_i)\overline{dd}_i]^2} \quad (21)$$

The ‘average-over-models’ estimate of that parameter is then given by

$$\overline{P} = \frac{\sum_i w_i P_i}{\sum_i w_i} \quad (22)$$

while the model-averaged estimate of the uncertainty in that parameter is calculated as the square root of the sum of the squares (SRSS) of the 95% confidence limit uncertainty in the (above) average of the parameter values and the average of the 95% confidence limit uncertainties yielded by the individual fits:⁷⁰

$$\overline{u}(\overline{P}) = \sqrt{f_{95}(N-1)^2 \frac{\sum_i [w_i(P_i - \overline{P})]^2}{\sum_i w_i} + \left[\frac{\sum_i [w_i u(P_i)]}{\sum_i w_i} \right]^2} \quad (23)$$

in which $f_{95}(m)$ (≈ 2) is the Student’s t -factor corresponding to a 95% confidence interval for m degrees of freedom.⁷¹ Application of this scheme to all of the 21 models whose \overline{dd} values lie within 2% of the lowest value attained (shaded region in the bottom panel of Figure 9) yielded overall estimated uncertainties $\overline{u}(\mathcal{D}_e) = 0.80 \text{ cm}^{-1}$ and $\overline{u}(r_e) = 0.000\,000\,73 \text{ Å}$. It should be noted, however, that while the average values of \mathcal{D}_e and r_e yielded by eq 22 (dotted lines in the upper panels of Figure 9) lie well outside the uncertainties in the parameter values associated with the recommended “best-fit” model (circled points in Figure 9), these differences are well within the overall uncertainty ranges (shaded regions centered on the results for the recommended best-fit model in the upper panels of Figure 9). It should also be noted that if the averaging had included all of the 32 models whose \overline{dd} values lie within 5% of their minimum, these estimated uncertainties would have increased only to 1.15 cm^{-1} and $0.000\,000\,81 \text{ Å}$, respectively, while if it had been restricted to the 15 models whose \overline{dd} values lie within 1% of the minimum, these uncertainties would have decreased to 0.78 cm^{-1} and $0.000\,000\,74 \text{ Å}$, respectively.

Figure 12 presents a plot of the MLR_{S,4}^{2,74}(12) potential energy function and shows the locations of all bound vibrational levels of the ^{24}MgH and ^{24}MgD isotopologues. The inset shows the distinct differences in the energies at the potential minima for ^{24}MgH and ^{24}MgD on an expanded scale. However, even on this scale, the -0.00024 Å shift of the position of the deuteride minimum relative to that of the hydride (see eq 29 of ref 42) is

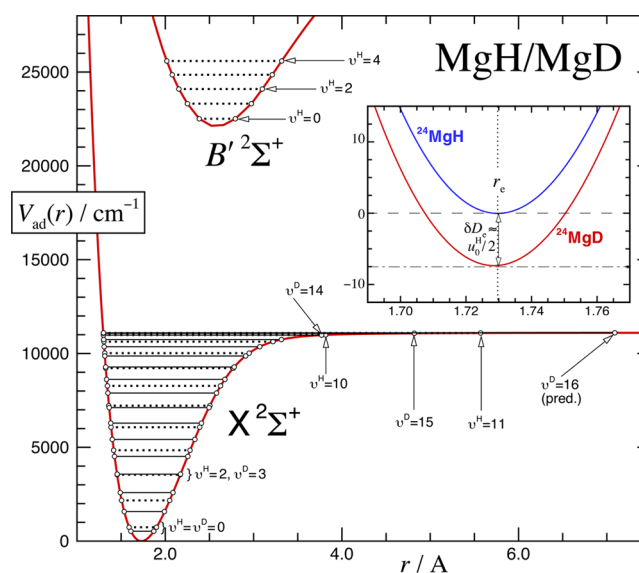


Figure 12. Plot of the ground-state potential energy curves for MgH and MgD (indistinguishable on this scale) showing the energies and turning points for all of the bound vibrational levels (dotted lines for MgH and solid lines for MgD) as well as turning points for the first five levels of the $B' \, ^2\Sigma^+$ state. Inset: Details of the ground-state hydride and deuteride potentials near their minima on an enlarged scale; very little shift in the equilibrium internuclear distance is evident.

not discernible. Predictions for the analogous MgT isotopologues show that their highest bound level is $v = 20$, which is bound by only 0.035 , 0.068 , and 0.110 cm^{-1} for ^{24}MgT , ^{25}MgT , and ^{26}MgT , respectively. Listings of the binding energies and band constants of all vibrational levels of all six isotopologues are given in the Supporting Information.

For illustrative purposes, Figure 12 also shows an RKR potential curve for the $B' \, ^2\Sigma^+$ state in this figure, taken from ref 72. This shows the radial displacement of the excited-state potential that led to our observations of so many transitions involving the higher vibrational levels of the ground state originating from the five lowest levels in the $B' \, ^2\Sigma^+$ state.

V. DISCUSSION

One feature of the final recommended Hamiltonian model that may seem somewhat less than ideal is the need for more parameters in the polynomial that defines the H-atom potential-energy BOB correction $\tilde{S}_{\text{ad}}^{\text{H}}(r)$ of eq 15 than are required to define the exponent polynomial $\beta(r)$ of eq 8 that defines the shape of the potential energy function itself. In an attempt to address this point, we experimented with the use of a radial expansion variable for $\tilde{S}_{\text{ad}}^{\text{H}}(r)$ defined in terms of an independent expansion center $r_{\text{ref}}^{\text{ad}}$. However, while this did allow us to obtain good fits with lower-order $\tilde{S}_{\text{ad}}^{\text{H}}(r)$ polynomials, the reduction was not enough to justify the additional complexity of the model. Moreover, when one includes \mathcal{D}_e , r_e , r_{ref} , q , and N_β , the number of parameters required to define the $\tilde{S}_{\text{ad}}^{\text{H}}(r)$ function of Table 4 (14) is fewer than that required to define the ^{24}MgH MLR potential, and this combined model also allows us to make reliable predictions for all of the tritium isotopologues. Thus, we conclude that our representation of the $\tilde{S}_{\text{ad}}^{\text{H}}(r)$ function by a 14-term polynomial in $y_4^{\text{eq}}(r)$ is indeed appropriate.

Figure 10 shows that the recommended potential does indeed approach the expected limiting C_6/C_8 behavior in the

limit as $r \rightarrow \infty$ ($1/r^2 \rightarrow 0$). However, the dip below the theoretical C_6/C_8 line in the region between the outer turning points for $\nu = 8$ and $\nu = 11$ is an interesting indicator of the nature of the intermolecular forces in this region. In particular, while the top panel of Figure 10 shows that the potential itself is smooth and monotonically attractive there, the $C_6^{\text{eff}}(r)$ plots show that at distances shorter than about 5.5 Å the growth of the attractive potential is substantially slower than any plausible extrapolation of the limiting dispersion energy behavior would lead us to expect. Moreover, the fact that in this region lie the outer turning points of the $\nu = 9$ –11 levels, which are associated with some 294 experimental data, means that this behavior is not some artefact of our model for the potential energy function.

In conclusion, inclusion of the new MgD data reported herein in a global DPF analysis has allowed us to obtain a better overall description of all of the isotopologues of the ground $X^2\Sigma^+$ state of MgH. A new model-averaged estimate of the ^{24}MgH well depth has been determined to be $D_e = 11104.25 \pm 0.80 \text{ cm}^{-1}$, in which the uncertainty takes account of averaging over a range of physically acceptable models. In addition, BOB radial strength functions indicate that the deuteride potential well is $7.58 \pm 0.30 \text{ cm}^{-1}$ deeper than that of the hydride.

■ ASSOCIATED CONTENT

● Supporting Information

Complete lists of the spectroscopic data used in the present analysis, the 2382 $B^2\Pi$ and $B'^2\Sigma^+$ term values determined in the final fit, and the first eight band constants (G_v , B_v , $-D_v$, H_v , ...) and $^2\Sigma$ splitting parameters [$\gamma_v^{(a)}$] for all of the bound levels of all nine isotopologues of ground-state MgH implied by the present radial Hamiltonian, together with a Fortran subroutine for generating the potential energy and centrifugal potential function for any MgH isotopologue. This material is available free of charge via the Internet at <http://pubs.acs.org>.

■ AUTHOR INFORMATION

Corresponding Authors

*E-mail: rdehende@uwaterloo.ca.

*E-mail: leroy@uwaterloo.ca.

Present Addresses

[§]A.S.: School of Chemistry, College of Science, University of Tehran, Tehran 14176, Iran.

^{||}P.F.B.: Department of Chemistry and Biochemistry, Old Dominion University, Norfolk, VA 23529, USA.

Notes

The authors declare no competing financial interest.

■ ACKNOWLEDGMENTS

Financial support for this work was provided by the Natural Sciences and Engineering Research Council (NSERC) of Canada through Undergraduate Student Research Awards (USRAs) to R.D.E.H. and C.C.H. and Discovery Grants to R.J.L.R. and P.F.B. We also gratefully acknowledge the very careful reading and critical comments on details of the manuscript provided by the referees and by Professor F. R. W. McCourt.

■ REFERENCES

- (1) Fowler, A. The Origin of Certain Bands in the Spectra of Sunspots. *Mon. Not. R. Astron. Soc.* **1907**, 67, 530–534.
- (2) Wallace, L.; Hinkle, K.; Li, G.; Bernath, P. The $\text{MgH } B'^2\Sigma^+ - X^2\Sigma^+$ Transition: A New Tool for Studying Magnesium Isotope Abundances. *Astrophys. J.* **1999**, 524, 454–461.
- (3) Gay, P. L.; Lambert, D. L. The Isotopic Abundances of Magnesium in Stars. *Astrophys. J.* **2000**, 533, 260–270.
- (4) Bonnell, J. T.; Bell, R. A. Further Determinations of the Gravities of Cool Giant Stars Using MgI and MgH Features. *Mon. Not. R. Astron. Soc.* **1993**, 264, 334–344.
- (5) Bernath, P. F.; Black, J. H.; Brault, J. W. The spectrum of magnesium hydride. *Astrophys. J.* **1985**, 298, 375–381.
- (6) Watson, W. W.; Rudnick, P. The Magnesium Hydride Band Spectrum. *Astrophys. J.* **1926**, 63, 20–32.
- (7) Watson, W. W.; Rudnick, P. Rotational Terms in the MgH Bands. *Phys. Rev.* **1927**, 29, 413–418.
- (8) Watson, W. W.; Perkins, B. Zeeman Effect in the Band Spectra of AgH, AlH, ZnH, and MgH. *Phys. Rev.* **1927**, 30, 592–597.
- (9) Mulliken, R. S. Electronic States and Band Spectrum Structure in Diatomic Molecules. VII. $^2P \rightarrow ^2S$ and $^2S \rightarrow ^2P$ Transitions. *Phys. Rev.* **1928**, 32, 388–416.
- (10) Pearse, R. W. B. The Ultra-Violet Spectrum of Magnesium Hydride. 1. The Band at $\lambda \approx 2430$. *Proc. R. Soc. London, Ser. A* **1929**, 122, 442–455.
- (11) Guntch, A. Neue Untersuchungen über das Bandenspektrum des Magnesiumhydrids. *Z. Physik* **1937**, 104, 584–591.
- (12) Guntch, A. Über Einige Neue Banden des Magnesiumhydrids. *Z. Physik* **1937**, 107, 420–424.
- (13) Turner, L. A.; Harris, W. T. The Ultraviolet Bands of Magnesium Hydride. *Phys. Rev.* **1937**, 52, 626–630.
- (14) Khan, M. A. Ultraviolet Spectrum of MgH and MgD. *Proc. Phys. Soc.* **1963**, 82, 572–580.
- (15) Balfour, W. J. The Electronic Spectrum of Magnesium Hydride and Magnesium Deuteride. *J. Phys. B: At., Mol. Opt. Phys.* **1970**, 3, 1749–1756.
- (16) Balfour, W. J. The $A^2\Pi \rightarrow ^2\Sigma^+$ Systems of ^{24}MgH , ^{25}MgH , and ^{26}MgH . *Astrophys. J.* **1970**, 162, 1031.
- (17) Balfour, W. J.; Cartwright, H. M. The ground state and $A^2\Pi$ excited state of magnesium deuteride. *Can. J. Phys.* **1975**, 53, 1477–1482.
- (18) Balfour, W. J.; Cartwright, H. M. Low-lying Electronic States of Magnesium Hydride. *Chem. Phys. Lett.* **1975**, 32, 82–85.
- (19) Balfour, W. J.; Cartwright, H. M. The $B'^2\Sigma^+ - X^2\Sigma^+$ Systems of MgH and MgD. *Can. J. Phys.* **1976**, 54, 1898–1904.
- (20) Balfour, W. J.; Cartwright, H. M. The $A^2\Pi - X^2\Sigma^+$ System and Dissociation Energy of Magnesium Hydride. *Astron. Astrophys., Suppl. Ser.* **1976**, 26, 389–397.
- (21) Balfour, W. J.; Lindgren, B. High-resolution emission spectra of MgH and MgD in the 600 to 850 nm wavelength region. *Can. J. Phys.* **1978**, 56, 767.
- (22) Balfour, W. J. MgH and MgD spectra in the 230–235-nm region. *J. Mol. Spectrosc.* **1980**, 79, 507–511.
- (23) Meyer, W.; Rosmus, P. PNO-CI and CEPA studies of electron correlation effects. III. Spectroscopic constants and dipole moment functions for the ground states of the first-row and second-row diatomic hydrides. *J. Chem. Phys.* **1975**, 63, 2356–2375.
- (24) Shayesteh, A.; Appadoo, D. R. T.; Gordon, I.; Le Roy, R. J.; Bernath, P. F. Fourier transform Infrared Emission Spectra of MgH and MgD. *J. Chem. Phys.* **2004**, 120, 10002–10008.
- (25) Leopold, K. R.; Zink, L. R.; Evenson, K. M.; Jennings, D. A.; Mizushima, M. The far infrared spectrum of magnesium hydride. *J. Chem. Phys.* **1986**, 84, 1935–1937.
- (26) Lemoine, B.; Demuynck, C.; Destombes, J. L.; Davies, P. B. Infrared diode laser spectra of MgH and MgD ($X^2\Sigma^+$). *J. Chem. Phys.* **1988**, 89, 673–677.
- (27) Zink, L. R.; Jennings, D. A.; Evenson, K. M.; Leopold, K. R. Laboratory measurements for the astrophysical identification of MgH. *Astrophys. J. Lett.* **1990**, 359, L65.
- (28) Ziurys, L. M.; Barclay, W. L., Jr.; Anderson, M. A. The millimeter-wave spectrum of the MgH and MgD radicals. *Astrophys. J. Lett.* **1993**, 402, L21–L24.

- (29) Shayesteh, A.; Henderson, R. D. E.; Le Roy, R. J.; Bernath, P. F. Ground State Potential Energy Curve and Dissociation Energy of MgH. *J. Phys. Chem. A* **2007**, *111*, 12495–12505.
- (30) GharibNezhad, E.; Shayesteh, A.; Bernath, P. Einstein A coefficients for rovibrational lines of the $A^2\Pi \rightarrow X^2\Sigma^+$ and $B'^2\Sigma^+ \rightarrow X^2\Sigma^+$ transitions of MgH. *Mon. Not. R. Astron. Soc.* **2013**, *432*, 2043–2047.
- (31) Hirao, T.; Pinchemel, B.; Bernath, P. F. The Rotational Analysis of the $A^2\Pi_r - X^2\Sigma^+$ Band System of MgBr. *J. Mol. Spectrosc.* **2000**, *202*, 213–222.
- (32) Norlén, G. Wavelengths and Energy Levels of Ar I and Ar II Based on New Interferometric Measurements in the Region 3400–9800 Å. *Phys. Scr.* **1973**, *8*, 249–268.
- (33) Whaling, W.; Anderson, W. H. C.; Carle, M. T.; Brault, J. W.; Zarem, H. A. Argon I lines produced in a hollow cathode source, 332 to 5865 nm. *J. Res. Natl. Inst. Stand. Technol.* **2002**, *107*, 149–169.
- (34) Le Roy, R. J. *DParFit: A Computer Program for Fitting Multi-Isotopologue Diatomic Molecule Spectra*, version 3.3; University of Waterloo Chemical Physics Research Report CP-660; University of Waterloo: Waterloo, ON, 2005; available at <http://leroy.uwaterloo.ca/programs/> (accessed Oct 17, 2013).
- (35) Le Roy, R. J.; Seto, J.; Huang, Y. *DPotFit: A Computer Program for Fitting Diatomic Molecule Spectra to Potential Energy Functions*, version 2.0; University of Waterloo Chemical Physics Research Report CP-667; University of Waterloo: Waterloo, ON, 2013; available at <http://leroy.uwaterloo.ca/programs/> (accessed Oct 17, 2013).
- (36) Watson, J. K. G. The Isotope Dependence of Diatomic Dunham Constants. *J. Mol. Spectrosc.* **1980**, *80*, 411–421.
- (37) Watson, J. K. G. The inversion of diatomic Born–Oppenheimer breakdown correction functions. *J. Mol. Spectrosc.* **2004**, *223*, 39–50.
- (38) Le Roy, R. J. Improved Parameterization for Diatomic Born–Oppenheimer Breakdown Effects and a New Combined-Isotopomer Analysis for HF and DF. *J. Mol. Spectrosc.* **1999**, *194*, 189–196.
- (39) Huang, Y.; Le Roy, R. J. Potential Energy, A Doubling and Born–Oppenheimer Breakdown Functions for the $B^1\Pi_u$ “Barrier” State of Li_2 . *J. Chem. Phys.* **2003**, *119*, 7398–7416; Erratum: **2007**, *126*, No. 169904.
- (40) Bernath, P. F. *Spectra of Atoms and Molecules*, 2nd ed.; Oxford University Press: New York, 2005.
- (41) Le Roy, R. J.; Henderson, R. D. E. A New Potential Function Form Incorporating Extended Long-Range Behaviour: Application to Ground-State Ca_2 . *Mol. Phys.* **2007**, *105*, 663–677.
- (42) Le Roy, R. J.; Dattani, N.; Coxon, J. A.; Ross, A. J.; Crozet, P.; Linton, C. Accurate Analytic Potentials for $\text{Li}_2(X^1\Sigma_g^+)$ and $\text{Li}_2(A^1\Sigma_u^+)$ from 2–90 Å, and the Radiative Lifetime of $\text{Li}(2p)$. *J. Chem. Phys.* **2009**, *131*, No. 204309.
- (43) Le Roy, R. J.; Haugen, C. C.; Tao, J.; Li, H. Long-range damping functions improve the short-range behaviour of an “MLR” potential energy curve. *Mol. Phys.* **2011**, *109*, 435–446.
- (44) Margenau, H. Van der Waals Forces. *Rev. Mod. Phys.* **1939**, *11*, 1–35.
- (45) Hirschfelder, J. O.; Curtiss, C. F.; Bird, R. B. *Molecular Theory of Gases and Liquids*; Wiley: New York, 1964.
- (46) Hirschfelder, J. O.; Meath, W. J. The Nature of Intermolecular Forces. In *Intermolecular Forces*; Hirschfelder, J. O., Ed.; Advances in Chemical Physics, Vol. 12; Interscience: New York, 1967; Chapter 1, pp 3–106.
- (47) Meath, W. J. The Structure of the Multipole Treatment of Intermolecular Forces. *Am. J. Phys.* **1972**, *40*, 21–27.
- (48) Le Roy, R. J.; Bernstein, R. B. Dissociation energy and long-range potential of diatomic molecules from vibrational spacings of higher levels. *J. Chem. Phys.* **1970**, *52*, 3869–3879.
- (49) Le Roy, R. J. Determining Equilibrium Structures and Potential Energy Functions for Diatomic Molecules. In *Equilibrium Structures of Molecules*; Demaison, J., Csaszar, A. G., Eds.; Taylor & Francis: London, 2011; Chapter 6, pp 159–203.
- (50) Le Roy, R. J. Long-range potential coefficients from RKR turning points: C_6 and C_8 for $B(^3\Pi_{0u}^+)$ -state Cl_2 , Br_2 , and I_2 . *Can. J. Phys.* **1974**, *52*, 246–256.
- (51) Ji, B.; Tsai, C.-C.; Stwalley, W. C. Proposed modification of the criterion for the region of validity of the inverse-power expansion in long-range potentials. *Chem. Phys. Lett.* **1995**, *236*, 242–246.
- (52) Dattani, N.; Le Roy, R. J. A DPF analysis yields accurate analytic potentials for $\text{Li}_2(a^3\Sigma_u^+)$ and $\text{Li}_2(c^1\Sigma_g^+)$ which incorporate 3-state mixing near the $c(1^3\Sigma_g^+)$ -state asymptote. *J. Mol. Spectrosc.* **2011**, *268*, 199–210.
- (53) It should be noted, however, that if the value of q is too small, say $q = 1$ or (sometimes also) 2, the MLR form sometimes displays unphysical behavior at short distances ($r < r_c$) or at large r outside the data-sensitive region.
- (54) Kreek, H.; Meath, W. J. Charge Overlap Effects. Dispersion and Induction Forces. *J. Chem. Phys.* **1969**, *50*, 2289–2302.
- (55) Douketis, C.; Scoles, G.; Marchetti, S.; Zen, M.; Thakkar, A. J. Intermolecular forces via hybrid Hartree–Fock-SCF plus damped dispersion (HFD) energy calculations. An improved spherical model. *J. Chem. Phys.* **1982**, *76*, 3057–3063.
- (56) Coxon, J. A. Born–Oppenheimer Breakdown Effects in the Determination of Diatomic Internuclear Potentials: Application of a Least-Squares Fitting Procedure to the HCl Molecule. *J. Mol. Spectrosc.* **1986**, *117*, 361–387.
- (57) Coxon, J. A. Application of an Improved Fitting Procedure for Diatomic Internuclear Potentials and Born–Oppenheimer Breakdown Functions: The $B^1\Sigma^+ \rightarrow X^1\Sigma^+$ System of H^{35}Cl and H^{37}Cl . *J. Mol. Spectrosc.* **1989**, *133*, 96–115.
- (58) Coxon, J. A.; Hajigeorgiou, P. G. The radial Hamiltonians for the $X^1\Sigma^+$ and $B^1\Sigma^+$ States of HCl. *J. Mol. Spectrosc.* **2000**, *203*, 49–64.
- (59) Coxon, J. A.; Dickinson, C. S. Application of direct potential fitting to line position data for the $X^1\Sigma^+$ and $A^1\Sigma^+$ states of LiH. *J. Chem. Phys.* **2004**, *121*, 9378–9388.
- (60) Le Roy, R. J.; Appadoo, D. R. T.; Anderson, K.; Shayesteh, A.; Gordon, I. E.; Bernath, P. F. Direct-potential-fit analysis of new infrared and visible $A^1\Sigma^+ - X^1\Sigma^+$ emission spectra of AgH and AgD. *J. Chem. Phys.* **2005**, *123*, No. 204304.
- (61) Coxon, J. A.; Hajigeorgiou, P. G. The $B^1\Sigma^+$ and $X^1\Sigma^+$ Electronic States of Hydrogen Fluoride: A Direct Potential Fit Analysis. *J. Phys. Chem. A* **2006**, *110*, 6261–6270.
- (62) Le Roy, R. J.; Appadoo, D. R. T.; Colin, R.; Bernath, P. F. On the $X^1\Sigma^+$, $A^2\Pi$ and $C^2\Sigma^+$ States of BeH, BeD and BeT. *J. Mol. Spectrosc.* **2006**, *236*, 178–188.
- (63) Coxon, J. A.; Hajigeorgiou, P. G. Direct potential fit analysis of the $X^1\Sigma^+$ ground state of CO. *J. Chem. Phys.* **2004**, *121*, 2992–3008.
- (64) Coxon, J. A.; Melville, T. C. Application of direct potential fitting to line position data for the $X^1\Sigma_g^+$ and $A^1\Sigma_u^+$ states of Li_2 . *J. Mol. Spectrosc.* **2006**, *235*, 235–247.
- (65) Le Roy, R. J.; Huang, Y. Representing Born–Oppenheimer Breakdown Radial Correction Functions for Diatomic Molecules. *J. Mol. Struct.: THEOCHEM* **2002**, *591*, 175–187.
- (66) Le Roy, R. J. *Level: A Computer Program for Solving the Radial Schrödinger Equation for Bound and Quasibound Levels*, version 8.0; University of Waterloo Chemical Physics Research Report CP-663; University of Waterloo: Waterloo, ON, 2007; available at <http://leroy.uwaterloo.ca/programs/> (accessed Oct 17, 2013).
- (67) R. J. Le Roy, *RKR1: A Computer Program Implementing the First-Order RKR Method for Determining Diatomic Molecule Potential Energy Curves*, version 2.0; University of Waterloo Chemical Physics Research Report CP-657; University of Waterloo: Waterloo, ON, 2003; available at <http://leroy.uwaterloo.ca/programs/> (accessed Oct 17, 2013).
- (68) Le Roy, R. J. *betaFIT: A Computer Program to Fit Potential Function Points to Selected Analytic Functions*, version 2.1; University of Waterloo Chemical Physics Research Report CP-666; University of Waterloo: Waterloo, ON, 2013; available at <http://leroy.uwaterloo.ca/programs/> (accessed Oct 17, 2013).
- (69) Mitroy, J.; Zhang, J. Y. Long-range dispersion interactions of the low lying states of Mg with H, He, Ne, Ar, Kr and Xe. *Mol. Phys.* **2008**, *106*, 127–132.

(70) Le Roy, R. J. Near-dissociation expansions and dissociation energies for Mg^+ –(rare gas) dimers. *J. Chem. Phys.* **1994**, *101*, 10217–10228.

(71) Press, W. H.; Flannery, B. P.; Teukolsky, S.; Vetterling, W. T. *Numerical Recipes: The Art of Scientific Computing*; Cambridge University Press: Cambridge, U.K., 1986.

(72) Shayesteh, A.; Bernath, P. Rotational analysis and deperturbation of the $A\ ^2\Pi \rightarrow X\ ^2\Sigma^+$ and $B'\ ^2\Sigma^+ \rightarrow X\ ^2\Sigma^+$ emission spectra of MgH . *J. Chem. Phys.* **2011**, *135*, No. 094308.